Pool stratification and mixing induced by steam injection through spargers: CFD modelling of the PPOOLEX and PANDA experiments

Gallego-Marcos Ignacio, Kudinov Pavel, Villanueva Walter, Kapulla Ralf, Paranjape Sidharth, Paladino Domenico, Laine Jani, Puustinen Markku, Räsänen Antti, Pyy Lauri, Kotro Eetu

DOI: 10.1016/j.nucengdes.2019.03.011

Pool Stratification and Mixing Induced by Steam Injection through Spargers: CFD modelling of the PPOOLEX and PANDA experiments

Ignacio Gallego-Marcos[a], Pavel Kudinov[a], Walter Villanueva[b], Ralf Kapulla[c], Sidharth Paranjape[c], Domenico Paladino[c], Jani Laine[d], Markku Puustinen[d], Antti Räsänen[d], Lauri Pyy[d], Eetu Kotro[d]

[a] Royal Institute of Technology (KTH), Division of Nuclear Engineering, Stockholm, Sweden.
[b] Royal Institute of Technology (KTH), Division of Nuclear Power Safety, Stockholm, Sweden.
[c] Paul Scherrer Institute (PSI), Division of Nuclear Energy and Safety Research, Villigen, Switzerland
[d] Lappeenranta University of Technology (LUT), Unit of Nuclear Safety Research, Lappeenranta, Finland
E-mails: igm@kth.se, pkudinov@kth.se, walterv@kth.se, ralf.kapulla@psi.ch, sidharth.paranjape@psi.ch, domenico.paladino@psi.ch, jani.laine@lut.fi, markku.puustinen@lut.fi, antti.rasanen@lut.fi, lauri.pyy@lut.fi, eetu.kotro@lut.fi

ABSTRACT

Spargers are multi-hole injection pipes used in Boiling Water Reactors (BWR) and Generation III/III+ Pressurized Water Reactors (PWR) to condense steam in large water pools. During the steam injection, high pool surface temperatures induced by thermal stratification can lead to higher containment pressures compared with completely mixed pool conditions, the former posing a threat for plant safety. The Effective Heat Source (EHS) and Effective Momentum Source (EMS) models were previously developed and validated for the modelling of a steam injection through blowdown pipes. The goal of this paper is to extend the EHS/EMS model capabilities towards steam injection through multi-hole spargers. The models are implemented in ANSYS Fluent 17.0 Computational Fluid Dynamics (CFD) code and calibrated against the spargers experiments performed in the PPOOLEX and PANDA facilities, analysed by the authors in [1] (Gallego-Marcos, I., et al., 2018). CFD modelling guidelines are established for the adequate simulation of the pool behaviour. A new correlation is proposed to model the turbulent production and dissipation caused by buoyancy. Sensitivity studies addressing the effect of different assumptions on the effective momentum magnitude, profile, angle and turbulence are presented. Calibration of the effective momentum showed an inverse proportionality to the sub-cooling. Differences between the effective momentum calibrated for PPOOLEX and PANDA are discussed. Analysis of the calculated flow above the cold stratified layer showed that the erosion of the layer is induced by the action of turbulence rather than mean shear flow.

KEYWORDS

Thermocline, turbulence production buoyancy, Richardson, C_{3e} coefficient, oscillatory bubble regime.

HIGHLIGHTS

- Modelling of steam injection with effective heat and momentum sources in the liquid
- VOF model not adequate when buoyancy is important in the higher density phase
- New Richardson based correlation for the turbulence buoyancy terms
- Effective momentum of oscillatory bubble inversely proportional to the subcooling
- Slow erosion of the cold layer is dominated by turbulence rather than mean shear

NOMENCLATURE

A	Area
C	Condensation regime coefficient
$C_{1\varepsilon}, C_{2\varepsilon}, C_{3\varepsilon}, C_{\alpha}, C_{\beta}$	Closure coefficient for turbulence models
g	Gravitational acceleration
G	Steam mass flux
$\mathcal{G}$	Turbulence production due to buoyancy
h	Specific enthalpy
k	Turbulent kinetic energy
K	Jet spread constant
M	Momentum rate
$\dot{m}$	Mass flow rate
N	Number of cells
P	Pressure
$\mathcal{P}$	Turbulence production due to shear
Pr	Prandtl number
r	Radial coordinate
Ri	Gradient Richardson number
Q	Heat rate
t	Time
T	Temperature
$\mathcal{T}$	Turbulence transport
U	Mean flow velocity
u'	Fluctuating turbulent velocity
x, y	Coordinates perpendicular to gravity vector
z	Coordinate parallel to gravity vector
Greek symbols	
α	Injection angle
β	Thermal expansion coefficient
γ	Specific heat capacity ratio
Δ	Increment
ε	Turbulent dissipation
θ	Azimuthal coordinate centered around the sparger axis
μ	Dynamic viscosity
ν	Kinematic viscosity
ρ	Density
ω	Specific turbulent dissipation
Super- and sub-indices	
0	Conditions inside the sparger, reference value

∞	Downstream conditions
eff	Effective source of EHS/EMS models
i	Injection holes, tensor index
L	Liquid, laminar
p	Pool
s	Steam
sat	Saturation
th	Theoretical
T	Turbulent
~	Non-dimensional quantity

1. INTRODUCTION

Containment over-pressure induced by the steam released through the primary coolant circuit is avoided in some designs of Light Water Reactors by condensing the steam in a large water pool [2]. In Boiling Water Reactors (BWR), this pool is known as the Pressure Suppression Pool (PSP), and steam is injected through blowdown pipes, connected to the drywell, and spargers, connected to primary circuit through the relief valves system. Generation II Pressurized Water Reactors (PWR) do not use the pool condensation system due to their larger containment volume compared to BWRs, which is expected to accommodate large quantities of steam without inducing fast pressure increases. Generation III/III+ reactors such as the AP1000, APR1400 and EPR are built with a pool condensation system known as the In-containment Refuelling Water Storage Tank (IRWST), where steam is injected through spargers connected to the pressurizer.

During a steam injection into the suppression pool, the development of thermal stratification is of safety concern since it reduces the pool's capacity to actuate as a heat sink, leading to higher containment pressures compared with completely mixed pool conditions. This is due to the higher pool surface temperature, which results in a higher steam partial pressure in the gas space above the pool. An example of this behaviour was found in the fast pressure increase at Fukushima Daiichi Unit 3 during the operation of the Reactor Core Isolation Condenser (RCIC) [3, 4]. Based on a mixed pool assumption, lumped parameter codes under-estimated the maximum pressure by about 160 kPa. In contrast to this, the assumption of a thermally stratified pool showed a much better agreement, suggesting that stratification was the cause of the fast pressure increase [5].

In order to develop predictive capabilities for thermal stratification and mixing induced by steam injection into a pool, Li and Kudinov [6] introduced in 2010 the concept of Effective Heat Source (EHS) and Effective Momentum Source (EMS) models. The goal of these models is to predict the time-averaged heat and momentum transferred from the steam to the liquid during different condensation regimes. These sources can be added to any CFD type code to enable simulating the pool behavior using a single-phase liquid solver. For example, analysis of the Pressurized POOL Experiments (PPOOLEX) with blowdown pipes demonstrated that the effective momentum induced by the chugging regime can be determined based on the frequency and amplitude of the liquid level oscillations inside the pipe [7, 8]. Further development of the models was done to provide non-dimensional correlations for the frequency and amplitude as a function of the injection conditions and geometry of the system [9]. Implementation of the EHS/EMS models in the thermal-hydraulic code of GOTHIC and validation against a large set of experiments performed in the PPOOLEX facility showed very good agreement with the pool temperature and containment pressures [10, 11].

The goal of this paper is to develop EHS/EMS models for spargers, which are multi-hole injection pipes injecting flow radially outwards. To accomplish this goal, the first step was to design a set of experiments in the PPOOLEX [12] and PANDA [13] facilities to understand the physical phenomena governing the sparger injection transients. A detailed presentation of the scaling approach used to design the experiments and of the analysis of the experimental data can be found in [1]. In this paper, the results from [1] are used (i) to establish the modelling guidelines needed to simulate the pool behaviour during such transients using CFD, and (ii) to calibrate the EHS/EMS sources induced by the condensation regimes. The effective momentum was not measured directly in any of the PPOOLEX or PANDA experiments. Thus, it is assumed that the estimates are adequate if they can successfully reproduce the ThermoCouples (TC) and Particle Image Velocimetry (PIV) data obtained in the experiments.

Previous works related to the modelling of a steam blowdown into a pool used CFD to resolve the direct contact condensation phenomena. For example, works done by [14, 15, 16] using ANSYS Fluent and NEPTUNE_CFD have shown that the unsteady chugging oscillations can be captured when using adequate correlations for the Nusselt number for the steam condensation. However, the high computational cost of the simulations enabled only a maximum simulation time of 60 s which is far beyond the hour or day time-scales required for thermal stratification. Lumped and system codes with a much coarser mesh provide a better computational efficiency, but are inadequate for the prediction of 3D flow phenomena which are important for the resulting pool transients [17].

Pool modelling during a steam injection through spargers was performed in [18, 19, 20], where the concept of the Steam Condensation Region Model (SCRM) was used and implemented in the CFD code of ANSYS CFX. In the SCRM, equations for mass, momentum, and energy are solved in a control volume where steam is expected to condense completely. Single-phase liquid boundary conditions are subsequently applied at the boundaries of the condensation region to model the entrainment and axial flows of the liquid jets. The SCRM is based on the same general idea as the EHS/EMS models. That is, direct contact condensation is not resolved explicitly and only large-scale effects for the pool are modelled. Application of the SCRM to complete mixing transient has shown good agreement with the experimental data. However, applicability to thermal stratification and mixing transients has not yet been addressed.

2. EHS/EMS MODEL FOR SPARGERS

The EHS/EMS models compute the effective heat Q_{eff} and momentum M_{eff} sources induced by the steam injection as time averaged values using equations (1) and (2) respectively [7],

$$Q_{eff}(t) = \frac{1}{\Delta t} \int_{t-\Delta t}^{t} Q(\tau) d\tau \tag{1}$$

$$M_{eff}(t) = \frac{1}{\Delta t} \int_{t-\Delta t}^{t} M(\tau) d\tau \tag{2}$$

where the integrals represent the time-average of the instantaneous variations of the sources over a period Δt of time. These variations are due to the oscillatory nature of direct contact condensation. For example, the large scale motions of the liquid inside the pipe during the chugging regime, the small scale oscillatory bubble behavior at the sparger holes, etc.

The effective momentum depends on the condensation regime. At very low steam mass fluxes all the steam can condense inside the pipe. Single-phase liquid flowing out of the injection holes induces an accordingly small effective momentum, which is usually not able to mix a stratified pool. Higher steam mass fluxes

push the steam-water interface outside of the injection holes and lead to an unstable condensation in which large bubbles collapse and force liquid to rush from the pool into the pipes [21]. Work done in [7, 8] showed that the effective momentum induced by chugging is a function of the frequency and amplitude of the liquid level oscillations inside the pipe.

The momentum induced by condensation regimes where the steam-water interface remains outside the pipe was initially estimated in [22] using a momentum balance over a cylindrical control volume covering the condensing jet (SCRM model). With the assumptions of negligible drag forces, uniform pressure in the liquid, entrainment perpendicular to the axial flow direction, and taking averaged flow properties, the momentum balance was derived in [18, 20] as

$$\rho_s A_i U_s^2 + P_s A_i = \rho_L A_L U_L^2 + P_\infty A_i \tag{3}$$

where U is the mean flow velocity, P the pressure, A the injection hole area, and indices s and L depict the steam and liquid, respectively. Based on equation (3), the liquid momentum results in equation (4), which is denoted in this paper as a theoretical M_{th} momentum.

$$M_{th} = \rho_s A_i U_s^2 + (P_s - P_\infty) A_i \tag{4}$$

2.1. Sonic and sub-sonic condensation regimes

In a sonic regime, the pressure P_s in equation (4) can be computed with

$$\frac{P_s}{P_0} = \left(\frac{2}{\gamma + 1}\right)^{\frac{\gamma}{\gamma - 1}} \approx 0.53 \tag{5}$$

where P_0 is the steam pressure inside the sparger and γ the specific heat capacity ratio of the injected fluid [23]. If P_s is higher than the ambient pressure P_∞, the jet expands right after being released into the ambient [24]. This is known as an under-expanded jet. Since condensation is negligible during the expansion, the divergent shape of the steam cavity accelerates the steam to super-sonic conditions, causing a second shock wave at the end of the expansion region. Successive expansion-contraction waves can be formed as the ambient pressure is further reduced. At a certain distance, sub-sonic flow is recovered, and the vapor contracts while condensing to generate an overall jet shape known as *ellipsoidal jet*. Exit pressures P_s similar to P_∞ can reduce the length of the expansion region until no super-sonic effects are observed. This forces the jet to contract virtually from the beginning, hence the name of *conic jet*.

In conic and ellipsoidal jets, steam momentum is transferred to the liquid through the droplets entrained into the vapour core [25, 26]. Entrainment occurs through Kelvin-Helmholtz (KH) and Rayleigh-Taylor (RT) instabilities, triggered by the large shear forces and density differences at the steam-liquid interface. The liquid droplets are accelerated by the steam and become larger as steam condenses on their surface. After a certain distance, steam has condensed completely, and a single-phase liquid jet is obtained.

When the steam mass flux is reduced below ~300 kg/(m^{2}s) the flow enters into the sub-sonic region. Here, the pressure at the outlet of the injection hole becomes equal to the ambient pressure ($P_s \approx P_\infty$). The steam pressure inside the sparger P_0 can reach larger values than P_∞, but only to over-come the pressure losses through the injection holes and other compressibility effects [1, 27]

Compared to sonic jets, the lower steam fluxes lead to a reduction in the KH and RT instabilities at the steam-liquid interface, decreasing the amount of liquid droplets entrained into the vapor core. This leads to the so called *oscillatory cone jet* regime, in which steam bubbles unable to condense within the vapor core are detached from the tip of the jet to condense through a collapse [28, 29]. Further reductions of the steam mass flux reduce the entrainment of liquid droplets to a point where most of the condensation occurs at the detached bubbles. This corresponds to the *oscillatory bubble* regime [30].

Most of the PPOOLEX and PANDA experiments were performed in the oscillatory bubble regime [1]. Only one experiment was performed in the stable cone jet regime (PPOOLEX SPA-T1) and another one in the chugging regime (PPOOLEX SPA-T2). The latter being an unstable regime characterized by a larger oscillations of the liquid level inside the pipe.

The application of equation (4) to the oscillatory bubble regime is not expected to provide an adequate estimate of the effective momentum since it does not take into account the dominant mechanisms of growth, necking, and collapse of the bubbles. Deriving a model to compute the effective momentum of this process is beyond the scope of this work. As stated in the Section 1, it will be calibrated by comparing the pool response obtained in the experiments and in the simulations (Section 4.2). Nevertheless, the starting point for this calibration can be obtained with equation (4), modified for a sub-sonic regime. That is, using $P_s = P_\infty$ and obtaining the steam density as $\rho_s(P_\infty)$, resulting in

$$M_{eff} = C\rho_s A_i U_s^2 \tag{6}$$

where a condensation regime coefficient C has been introduced. As an example, the C values derived from [10] for the chugging regime in blowdown pipes varied between about 0.2 and 4, depending on the injection conditions and pipe diameter. The variables of P_∞, T_s, and $\dot{m}_s$, necessary to obtain the $\rho_s A_s U_s^2$ term in equation (6), were all measured in all PPOOLEX and PANDA experiments.

The effective heat source induced by all condensation regimes can be calculated with

$$Q_{eff} = \dot{m}_s(h_s - h_L) \tag{7}$$

where h_s is the steam enthalpy inside the sparger obtained from the experimental data and h_L the liquid enthalpy in the pool.

3. IMPLEMENTATION OF THE EHS/EMS MODELS IN FLUENT

In previous work done by the authors the EHS/EMS models for spargers were implemented in the thermal hydraulic code of GOTHIC. The results were in good agreement with the PPOOLEX experiments [31]. Nevertheless, it was found that the Cartesian mesh used by GOTHIC causes significant diffusion of the radial sparger jets not aligned with the mesh, and a focusing effect of those aligned with it. CFD codes such as ANSYS Fluent allow the generation of radial meshes which are more suitable for these conditions. Thus, in this work, we decided to implement the EHS/EMS models for spargers in ANSYS Fluent, version 17.0. In this section, we address some of the most important modelling options needed to capture the pool behaviour adequately. The sensitivity studies were based on the condition of the PANDA HP5-3 experiment, whose temperature evolution can be observed in Figure 22a.

3.1. Single-phase modelling

In the PPOOLEX and PANDA experiments the pool was in direct contact with an air space above it. Modelling of the gas and liquid phases in Fluent can be done by using the Eulerian-Eulerian models such

as Volume of Fluid (VOF), Mixture, and Eulerian. However, these multiphase models were found to be inadequate for our case. The reason for this is that Fluent (and most CFD codes) include a reference density ρ_o in the momentum equation to remove the hydrostatic head from the pressure [32], equation (8).

$$-\nabla P + \rho g_i = -\nabla(P - \rho_0 g_i x_i) + (\rho - \rho_0) g_i \tag{8}$$

This leads to a better sensitivity between pressure and velocity changes and improves the accuracy as well as the stability of the simulations. The main problem is that users can only define *one* reference density for both phases. Thus, we can only choose *one* phase to have zero hydrostatic pressure and accurate body forces. The Fluent manual recommends using the reference density of the lightest phase. However, as we can see in Figure 1a, this led to a poor prediction of the pool thermal behaviour, where the stable stratification observed in the experiments could not be captured. Using the reference density of the liquid enabled reproducing the pool thermal behaviour; but at the cost of causing a complete destabilization of the gas space, where unphysical high air velocities of 2 m/s were observed, requiring a very low time step to maintain stability (Figure 1b).

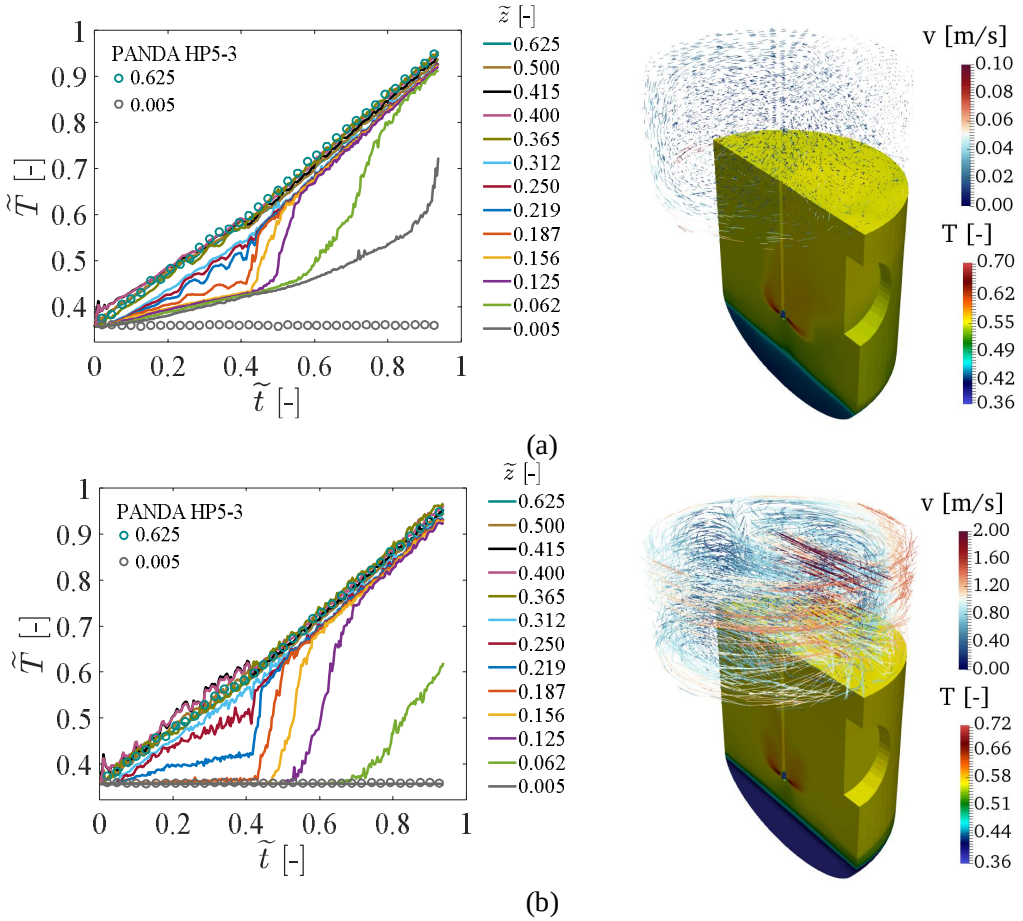

Figure 1: Temperature and velocity fields obtained with the VOF model using a reference density ρ_o of (a) 1.2 kg/m^3 (b) 990 kg/m^3. Full 3D, k-ω BSL with $C_{3\varepsilon}(Ri_g)$, non-uniform EHS/EMS, source term approach. Definition of these terms is given in Section 3. This applies for all the figures presented in this section. All relevant PANDA data is presented in non-dimensional form. This applies for all the figures presented in the paper.

The issue presented in Figure 1 is not specific to Fluent. Similar results were observed when implementing the model in STAR-CCM+. Private correspondence with ANSYS Fluent support agreed on the inadequacy of Eulerian models for simulations where body forces are of interest in the large density phase. Therefore, it was decided to simulate the pool alone using a single-phase solver. The pool surface was modelled as a shear-free wall and the liquid level was controlled with a User Defined Function (UDF) to increase with dynamic layering as a function of the added mass and density changes.

In PANDA, the total mass injected was negligible compared with the water inventory of the pool. Thus, a static mesh with zero mass injection also led to very similar results compared with using a dynamic mesh (Figure 2).

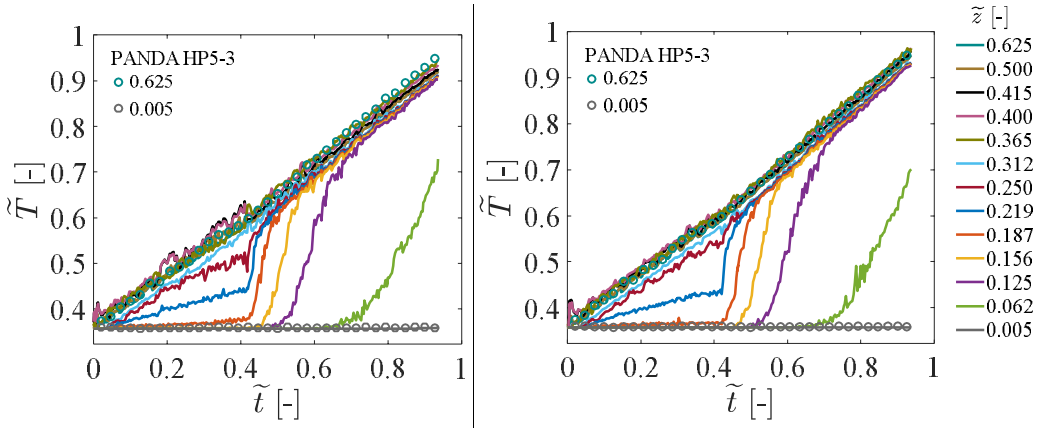

(a) (b)

Figure 2: Pool temperatures along a vertical line obtained with a single-phase solver using (a) dynamic and (b) static meshes. Full 3D, k-ω BSL with $C_{3\varepsilon}(Ri_g)$, non-uniform EHS/EMS, source term approach.

3.2. Buoyancy effects on mean flow

During the PPOOLEX and PANDA experiments, the temperature difference between the hot and cold layers varied between 15 to 30°C and the average pool temperatures between 15 to 90°C. The Boussinesq approximation for buoyancy

$$(\rho - \rho_0) g_i \approx -\rho_0 \beta (T - T_0) g_i \tag{9}$$

is valid for this case because $\beta(T - T_0) \ll 1$ holds true. However, the large temperature range requires using a temperature dependent thermal expansion coefficient β, since it increases by a factor of ~8 between 15 and 90°C. Unfortunately, Fluent does not allow to define a variable β. This causes an over or under-prediction of the buoyancy forces for temperatures below and above the reference β, respectively.

To solve this issue, buoyancy effects were considered by using a temperature-dependent density obtained from the fitting of the IAPWS water properties as

$$\rho = 1.6137 \cdot 10^{-5} T^3 - 0.019024 T^4 + 6.7867 T + 236.964 \tag{10}$$

where T is the water temperature in Kelvin.

For simplicity, all the sensitivity studies presented in this paper were run with the Boussinesq approximation and a constant β = 0.00045. However, the simulations used to calibrate the effective momentum (Section 4.2) were all run using a temperature-dependent density.

3.3. Buoyancy effects on turbulence

Stable stratification tend to dissipate vertical fluid motions through buoyancy effects, thereby reducing the heat and momentum transferred across the thermocline [33]. This effect was observed in all PPOOLEX and PANDA experiments, which showed that the cold layer remained at its initial temperature throughout the low and high steam injection phases [1]. From the modelling point of view, this behaviour poses two main difficulties. First, two-equation turbulence models are calibrated for fully turbulent flows. Application to laminar flows (i.e. quasi-stagnant cold layer) can cause over-predictions of the turbulent viscosity. This is especially problematic for k-ε models, equations (11) and (12), where the dissipation term in the ε equation tends to infinity as the turbulent kinetic energy k approaches zero.

$$\frac{D(\rho k)}{Dt} = \mathcal{P} + \mathcal{G} - \rho\varepsilon + \mathcal{T}_k \tag{11}$$

$$\frac{D(\rho \varepsilon)}{Dt} = C_{1\varepsilon}\frac{\varepsilon}{k}(\mathcal{P} + C_{3\varepsilon}\mathcal{G}) - C_{2\varepsilon}\rho\frac{\varepsilon^2}{k} + \mathcal{T}_\varepsilon \tag{12}$$

The thermal hydraulic code of GOTHIC limits the over-prediction of k-ε models by damping the turbulent viscosity to zero when the cell Reynolds number falls below 5000 [34]. Simulations performed by the authors using GOTHIC show that this damping enables reproducing the stable stratification observed in the sparger experiments [31]. Fluent does not have a Reynolds based limit. However, the k-ω models available in Fluent can solve this issue.

The k-ω models define a dissipation rate ω proportional to ε/k, which eliminates the division by k in the dissipation term, equation (13). This enables them to be applied all the way down to the boundary layer, and to limit the turbulent over-prediction at stagnation regions. Over-prediction due to high strain rates does not improve in comparison with k-ε models since both assume a $\mathcal{P} \propto S^2$. However, production limiters are available in Fluent to minimize this behavior [32].

$$\frac{D(\rho \omega)}{Dt} = C_\alpha\frac{\omega}{k}(\mathcal{P} + C_{3\varepsilon}\mathcal{G}) - C_\beta\rho\omega^2 + \mathcal{T}_\omega \tag{13}$$

The second important aspect for the modelling of a stratified pool is the turbulent production due to buoyancy $\mathcal{G}$. In Fluent, this term is present in the k-ε models, but not in the k-ω. Thus, it was included through a UDF when needed. The $\mathcal{G}$ term appears during the derivation of the k equation as $\overline{u_i'\rho'}$, and it is usually modelled using the Standard Gradient Diffusion Hypothesis (SGDH), equation (14). It becomes negative in stable stratification ($\partial T/\partial z > 0$, $g_i < 0$) and positive in unstable stratification ($\partial T/\partial z < 0$, $g_i < 0$).

$$\mathcal{G} = g_i\overline{u_i'\rho'} \approx g_i\left(\beta\frac{\mu_T}{Pr_T}\frac{\partial T}{\partial x_i}\right) \tag{14}$$

Since the ε and ω equations are built in analogy to the k equation, buoyancy terms should also be present there. However, contrary to the turbulent production term due to shear $\mathcal{P}$, the buoyancy term $\mathcal{G}$ can be positive or negative (acting as a producer or destroyer of k), questioning the need of a term in the ε and ω equations. For this reason, Fluent default setting is $C_{3\varepsilon} = 0$ [32]. However, there seems to be a consensus in the literature that $C_{3\varepsilon}$ should tend to 0 or 1 depending on whether we are in stable or unstable stratification conditions, respectively [35]. Fluent and other CFD codes to model this dependency as

$$C_{3\varepsilon} = \tanh\left|U_z / U_{xy}\right| \tag{15}$$

where U_z and U_{xy} are the velocity vectors parallel and perpendicular to the gravity vector, respectively [32]. In this work, we propose to model the $C_{3\varepsilon}$ parameter using the gradient Richardson number Ri_g.

$$Ri_g = \frac{\beta g \frac{\partial T}{\partial z}}{\left(\frac{\partial U_x}{\partial z}\right)^2 + \left(\frac{\partial U_y}{\partial z}\right)^2} \tag{16}$$

Theoretical [36, 37] and experimental [38, 39] works have shown that the transition from stable to unstable stratification occurs between $0.2 < Ri_g < 1$. Based on this, $C_{3\varepsilon}$ can be calculated as

$$C_{3\varepsilon} = \begin{cases} 0 & Ri_g > 1 \text{ (Stable)} \\ -1.25 Ri_g + 1.25 & 0.2 < Ri_g < 1 \text{ (Transition)} \\ 1 & Ri_g < 0.2 \text{ (Unstable)} \end{cases} \tag{17}$$

The assumption done in equation (15) is that any flow where $U_{xy} \gg U_z$ is in stable stratification. This is not necessarily the case. The jets induced by the sparger fulfill the $U_{xy} \gg U_z$ condition. However, their large velocities and temperature compared with the pool make them an unstable stratified flow, for which the $C_{3\varepsilon} \sim 1$ predicted by equation (17) is appropriate (Figure 3).

In the cold layer, the absence of a well-defined mean flow allows equations (15) and (17) to take any value between 0 and 1. Since equation (15) does not take temperature into account, the lower side of the thermocline is continuously diffused by overshoots of the turbulent viscosity when an inadequate $C_{3\varepsilon}$ =1 is predicted in this region. On the other hand, equation (17) is able to predict an adequate $C_{3\varepsilon}$ = 0 throughout the thermocline since $\partial T / \partial z \gg \partial U / \partial z$ (Figure 3). This provides an adequate "insulation" between the hot and cold layers, maintain the sharp interface between them observed in the experiments (Figure 4ab).

Overshoots of the turbulent viscosity were also observed at the lower side of the thermocline when using equation (17). However, they were very sporadic and did not cause a noticeable mixing between the layers. The main problem of these overshoots is on the numerical side, since they slow down the convergence of the calculation when present. Setting a constant $C_{3\varepsilon}$ = 0 (Figure 4c) led to no turbulent viscosity overshoots, whereas a constant $C_{3\varepsilon}$ = 1 (result not shown) lead to even more than when using equation (15). This result suggests that the overshoots are due to predicting an inadequate $C_{3\varepsilon}$ = 1 at the thermocline, which increases the turbulent viscosity by causing an unnecessary dissipation of ω. Indeed, sensitivity studies showed that convergence can be improved by modifying the Ri_g transition region in equation (17) from 0.2-1 to 0-1. In terms of pool behavior, these two simulations resulted in almost identical results. The modification of the Ri_g range to 0-1 agrees with the work done in [36, 37] in the sense that $Ri_g < 0.2$ is only a necessary condition to develop instability (which could occur at lower values); whereas $Ri_g > 1$ is a sufficient condition for stability.

Another aspect occurring in both $C_{3\varepsilon}$ models is the behaviour at the cold layer, far below the thermocline. Here, the absence of significant temperature and velocity gradients allow equations (15) and (17) to predict any $C_{3\varepsilon}$ value. Fortunately, the absence of these gradients also leads to a $\mathcal{G} \approx 0$, equation (14), avoiding any effect in the turbulent equations or overshoots of the turbulent viscosity.

Setting a constant $C_{3\varepsilon}$ = 0 produces better results than using equation (15) (Figure 4c). However, using $C_{3\varepsilon}$ = 0 is not recommended since sporadic over-turns of the flow with $\partial T/\partial z$<0 (unstable stratification) cannot induce a production of ω which would limit the turbulent viscosity. This was observed to cause over-estimations of the turbulent viscosity and a partial diffusion of the thermocline (Figure 4c). Using a constant $C_{3\varepsilon}$ = 1 (not included in the paper), showed an even stronger diffusion than what observed in Figure 4a.

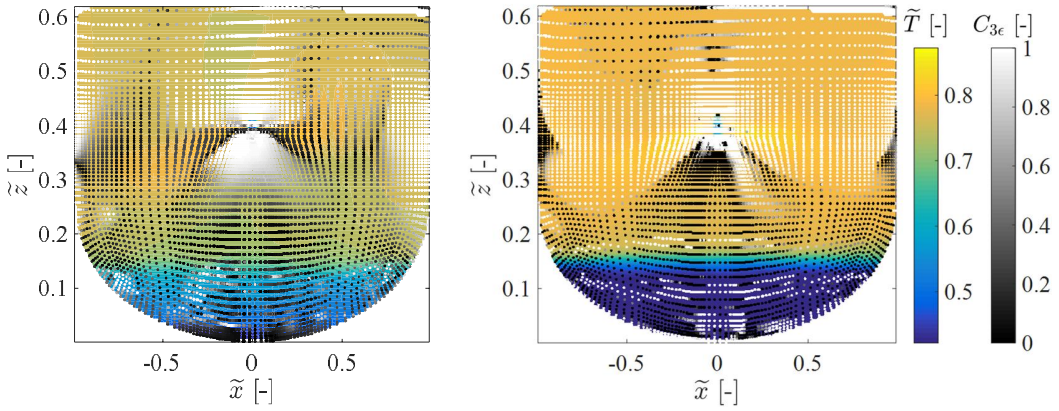

(a) (b)

Figure 3: Temperature contours and local $C_{3\varepsilon}$ values at $\tilde{t}$ = 0.48 as obtained from the simulations from (a) Figure 4a using $C_{3\varepsilon} = \tanh|U_z/U_{xy}|$ and (b) Figure 4b using $C_{3\varepsilon}(Ri_g)$ according equation (17). Note that only points below $\tilde{z}$ = 0.6 are included.

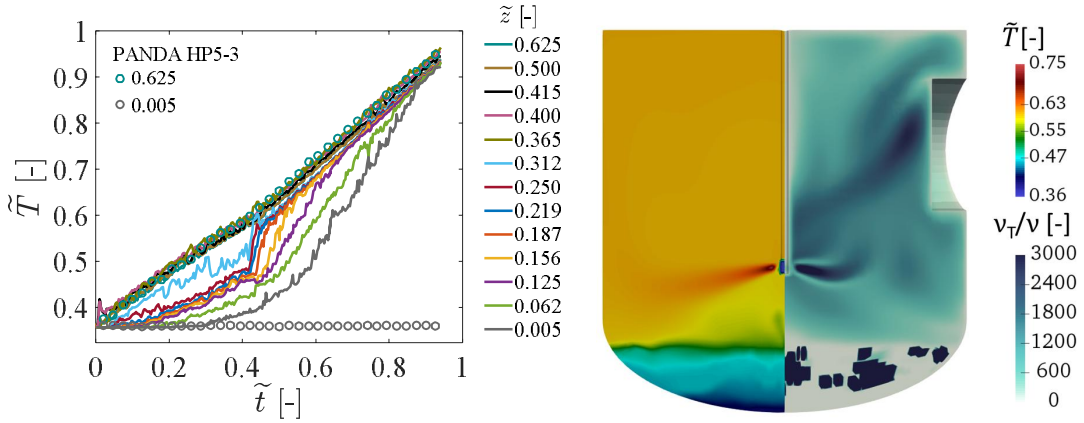

(a)

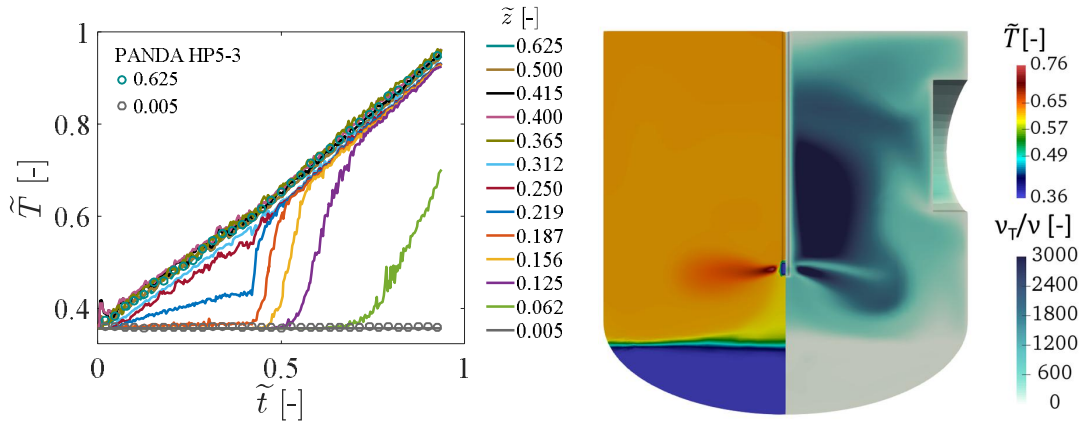

(b)

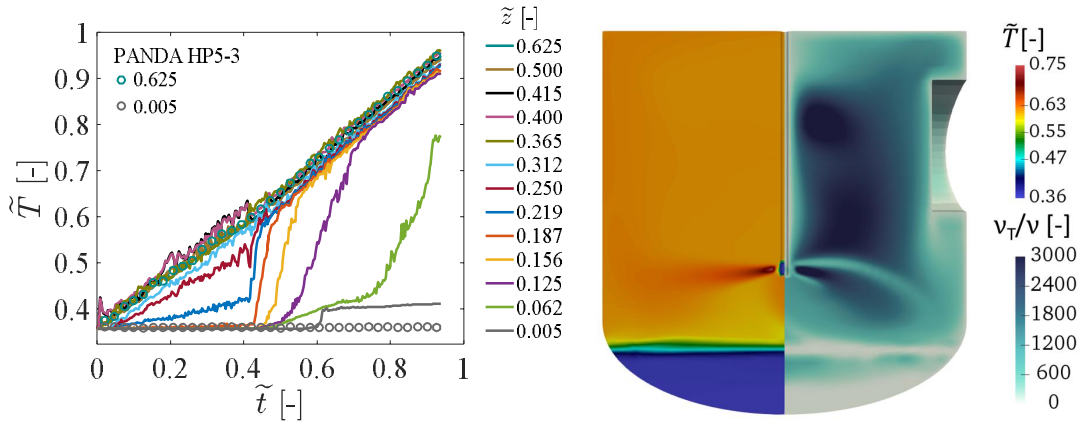

(c)

Figure 4: Pool temperatures along a vertical line and contours of the pool temperature and turbulent viscosity ratio (kinematic to turbulent viscosity) at $\tilde{t}$ = 0.48 obtained with the k-ω BSL turbulence model with (a) $C_{3\varepsilon} = \tanh\left|U_z / U_{xy}\right|$ (b) $C_{3\varepsilon}(Ri_g)$, and (c) $C_{3\varepsilon}$ = 0. Production limiters enabled. Full 3D, single-phase, non-uniform EHS/EMS, source term approach.

Simulations run with the k-ε Realizable model showed much larger over-prediction of the turbulent viscosity than k-ω models, regardless of the buoyancy terms used. As an example for this the results obtained when using the default Fluent setting of $C_{3\varepsilon}$ = 0 are presented in Figure 5. Compared to the k-ω BSL prediction using the same $C_{3\varepsilon}$ = 0 (Figure 4c), the over-prediction is clearly higher. Similar results were obtained when using the full buoyancy terms option (equation (15)), or using the $C_{3\varepsilon}$ model proposed in equations (16) and (17). A similar behavior was also obtained when decreasing the production limiter C_{lim} from 10 to 5. These results show the inadequacy of k-ε models for simulation involving stagnation regions. Based on these results, the simulations presented in Section 4 were run using the k-ω BSL model and a $C_{3\varepsilon}$ calculated with equations (16) and (17).

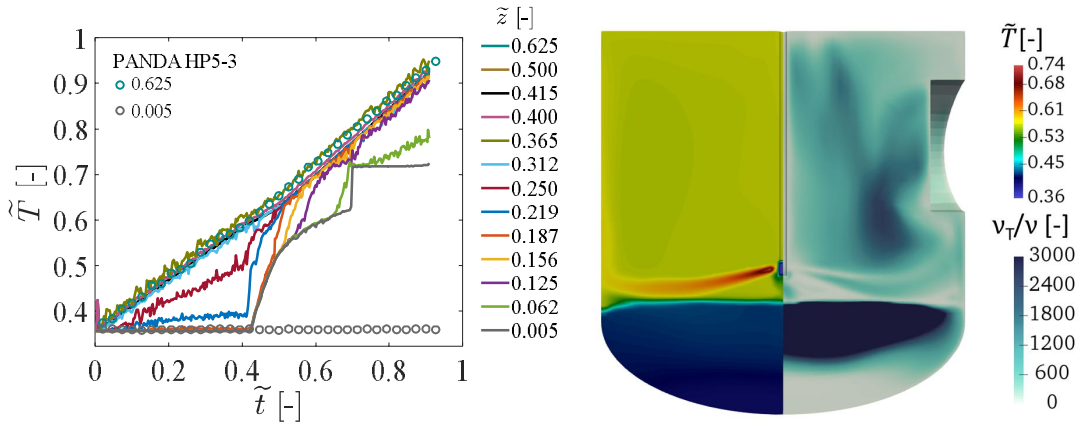

Figure 5: Pool temperatures along a vertical line and contours of the pool temperature and turbulent viscosity ratio obtained at $\tilde{t}$ = 0.51 obtained with the k-ε Realizable turbulence model with $C_{3\varepsilon}$ = 0. Production limiter enabled. Full 3D, single-phase, non-uniform EHS/EMS, source term approach.

3.4. Flow structure: 2D and 3D simulations

The flow structure generated by the steam injection was observed to require a 3D treatment. During the low steam injection phase, the buoyancy-dominated flow rises close to the sparger pipe towards the top of the pool and generates a clockwise circulation pattern above the cold layer (Figure 6b). During the high steam injection phase, the higher inertia of the jets dominates over buoyancy effects and was able to change this rotation to counter-clockwise (Figure 6c). 2D-axisymmetric simulations showed large flow instabilities during the transition between these two flow patterns [40, 41]. These instabilities are caused by the lower degrees of freedom of a 2D simulation, which prevent vortices to stretch and accommodate to changes in the flow, possible for a 3D simulation.

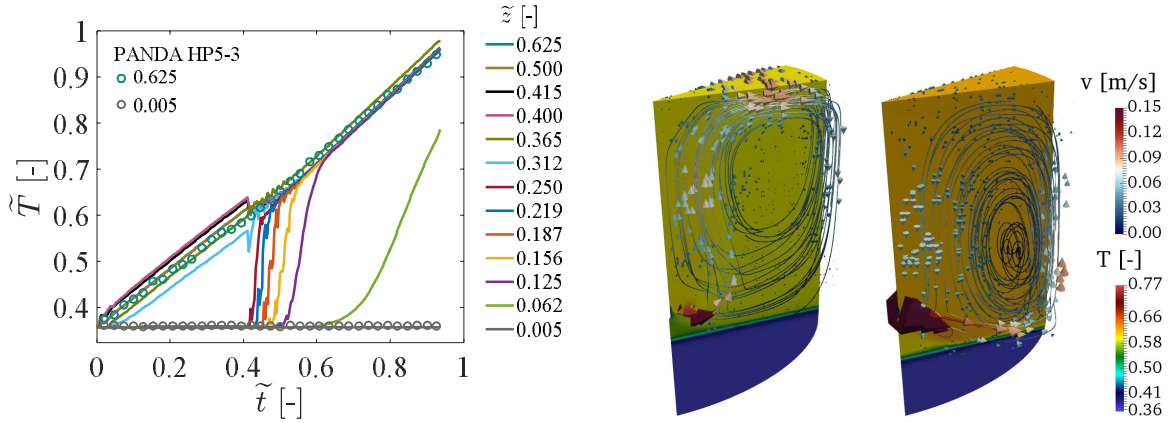

(a) (b) (c)

Figure 6: 3D slice model, 45°. (a) Pool temperatures along a vertical line and pool temperature and velocity field at (b) $\tilde{t}$ = 0.38 (low steam injection) and (c) $\tilde{t}$ = 0.46 (high steam injection). Single-phase, k-ω BSL with $C_{3\varepsilon}(Ri_g)$, non-uniform EHS/EMS, source term approach.

Another shortcoming of 2D-axisymmetric models is their implicit assumption of uniform momentum distribution in the azimuthal direction. Analysis of the sparger experiments done in [1] suggest possible non-uniformities in the azimuthal direction. Thus, a 3D slice of the pool is required to model this.

The slice simulation from Figure 6 showed good qualitative comparison to the experimental data. However, full 3D modelling of the pool showed that the Inter connecting Pipe (IP), slightly projecting beyond the inner surface of the vessel wall into the pool of the PANDA vessel, had a symmetry breaking effect and resulted in an increase of the unsteadiness of the flow (Figure 7). This caused a faster erosion of the cold layer during the low steam injection phase in comparison to what was predicted by the 45º slice simulation (see Figure 6 and Figure 4b). Therefore, the simulations from Section 4 were run using a full 3D model with non-uniform heat and momentum sources.

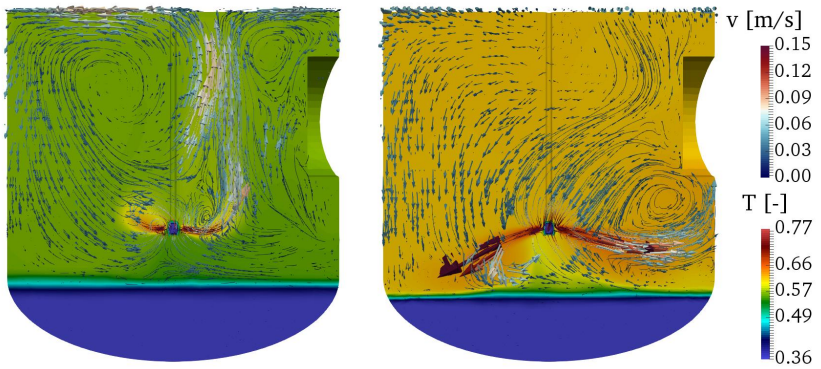

(a) (b)

Figure 7: Full 3D model, including Interconnecting Pipe (IP). Temperature and velocity fields at (a) $\tilde{t}$ = 0.38 (low steam injection) and (b) $\tilde{t}$ = 0.46 (high steam injection). Single-phase, k-ω BSL with $C_{3\varepsilon}(Ri_g)$, non-uniform EHS/EMS, source term approach.

3.5. Source term approach

The heat and momentum induced by a steam injection can be introduced in the simulation through boundary conditions or through source terms in the transport equations. The boundary condition approach (SCRM) was successfully applied in [18, 19, 20] to complete mixing transients induced by a sparger. On the other hand, source terms were successfully used in [8, 10, 11] to model stratification and mixing transients induced by blowdown pipes. Given the same heat and momentum sources, both approaches should produce the same pool behaviour. However, the simulations performed in this work showed some differences.

In the SCRM method the entrainment angle towards the sparger jets is user-defined. This angle should vary in time and space depending on the instantaneous flow field [42]. However, the simulations presented in [18, 19, 20] were run assuming a constant 90º angle, forcing the flow field to maintain a specific direction. This behaviour can be observed in Figure 8a, where we can see that with the SCRM the flow below the sparger is more upwards oriented compared with the source term approach, Figure 8b. In principle, the SCRM could be extended to compute the time-dependent angle for each cell at the condensation region. But the specific implementation of this model is beyond the scope of this paper.

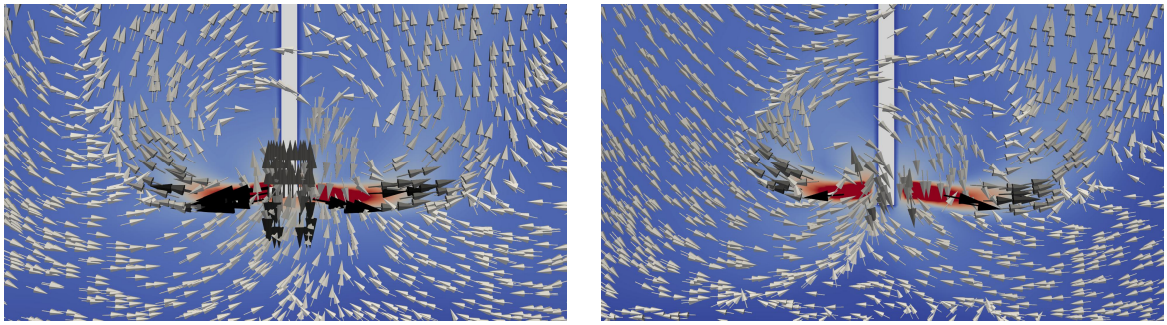

(a) (b)

Figure 8: Velocity vectors and contours time-averaged over the entire low steam injection phase. Results obtained with the (a) Steam Condensation Region Model (SCRM) with 90° entrainment and (b) source term approach. Full 3D, single-phase, k-ω BSL with $C_{3\varepsilon}(Ri_g)$, non-uniform EHS/EMS

Using the same effective heat and momentum as in Figure 4b, the pool behaviour obtained with the SCRM is presented in Figure 9. We can see that the upwards flow caused by the fixed 90° entrainment eroded the cold layer further down than in the source term simulation during the low steam injection phase. Since the effective momentum is an uncertain parameter, both approaches could be fitted to the experimental data by calibrating the C coefficient in equation (6). However, the issue with the fixed entrainment angle suggests that the estimate done with the source term would produce a more realistic value of C. For this reason, all of the simulations presented in Section 4 use the source term approach.

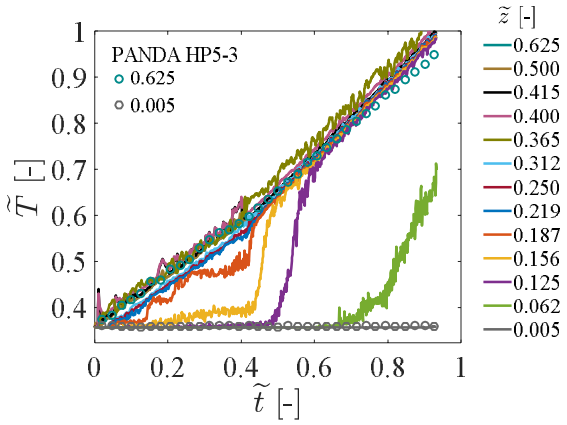

Figure 9: Pool temperatures along a vertical line obtained with the Steam Condensation Region Model (SCRM). Full 3D, single-phase, k-ω BSL with $C_{3\varepsilon}(Ri_g)$, non-uniform EHS/EMS.

4. CALIBRATION OF THE EHS/EMS MODEL PARAMETERS

In this section, we present the calibration of the EHS/EMS models for steam injection through spargers as presented in Sections 2 and 3 against the PANDA HP5-1, 2, and 3 and the PPOOLEX SPA-T3, T4, T5, and T6 experiments. The goal is to assess the influence of different injection conditions of injection angle, momentum profile and turbulent source; calibrate the C coefficient introduced in equation (6), and analyse the dependency of C on the different experimental conditions. The details of the numerical setup used in the Fluent simulations are given in Table 1. It should be noted that the compressible liquid formulation was only used in the simulations presented in Section 4.2, where the C coefficient from equation (6) is calibrated. The rest of the simulations were run using the Boussinesq approximation with a constant β = 0.00045.

Table 1: Mesh and numerical parameters used in the Fluent simulations for the PANDA and PPOOLEX experiments.

	PANDA	**PPOOLEX**
Mesh	Full 3D, 540 000 cells	Full 3D, 470 000 cells
	Dynamic layering at pool surface	
	ICEM quality data: worst/average values (0-1)	
	Determinant: 0.46/0.91 Skewness: 0.41/0.89 Orthogonality: 0.58/0.96	Determinant: 0.55/0.91 Skewness: 0.50/0.87 Orthogonality: 0.57/0.96
Phases	Single-phase liquid Compressible, equation (8)	
Turbulence model	k-ω BSL (Kato-Launder and Production Limiter enabled) UDF for buoyancy sources $C_{3\varepsilon}(Ri_g)$ according to equation (17) Wall functions y+ independent: max y+ 50-150	
EHS/EMS models	Equations (6) and (7), C coefficient calibrated with experiments Non-uniform heat and momentum sources (K = 40) No turbulence sources added 10^o downwards inclination of the jets	
Solver	PISO 1 neighboring and 1 skewness correction, coupled	
Pressure solver	Body Force Weighted	
Gradient scheme	Least Squares Cell Based	
Space interpolation	QUICK (all variables)	
Time scheme	Second Order Implicit	
Time step	0.02-0.1 s (max Courant 1)	
Residuals	10e-6 energy, 10e-5 rest	
Relaxation factors	0.7 pressure, 0.3 momentum High Order Term Relaxation 0.6 for all variables	

The equations for the jet spread proposed by the authors in [1] were used to compute the non-uniform heat and momentum sources of the EHS/EMS models. The sources were located in an annular region of 50×50 mm and 40×40 mm cross section for PANDA and PPOOLEX respectively, centred at the location of the sparger steam injection. The radius of the annulus centreline was 100 mm. The momentum profile for a specific steam injection condition and the resulting velocity field are presented in Figure 10a and Figure 10b, respectively.

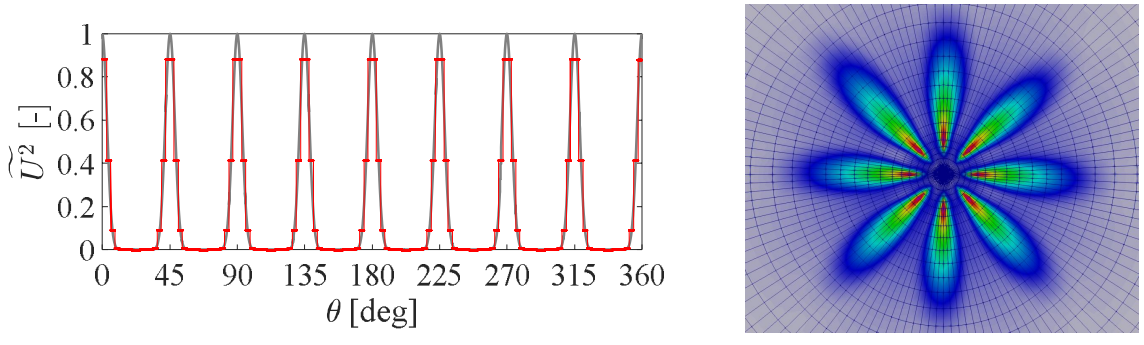

(a) (b)

Figure 10: (a) Profile of the non-uniform EHS/EMS sources and (b) velocity field obtained when using the N_θ 128 Δz 25 mesh (Table 2).

The mesh sensitivity study was done based on the PANDA HP5-2 experiment, to analyse the cell sizes in the vertical and azimuthal directions (Table 2). These cell sizes control the numerical temperature diffusion across the thermocline and the numerical velocity diffusion of the non-uniform jets generated by the sparger. We can see in Figure 12a that a decreased cell size in the vertical direction Δz leads to a sharper temperature gradient across the hot and cold layers. Mesh convergence is achieved best when the number of cells in the azimuthal direction is increased from 64 to 128, Figure 12b. Based on the results from Figure 12 and considering the computational time, it was decided to run the rest of the simulations using N_θ 128 Δz 25 mesh (Figure 11), which shows a similar qualitative behaviour as the experiments (Figure 12c).

Using 24 cores for the coarsest mesh and 144 for the finest, the CPU time was about 1 week for of each one of the simulations presented in Figure 12. The simulations performed with the selected N_θ 128 Δz 25 mesh were run in 48 cores.

Table 2: Cell parameters used in the mesh sensitivity study for the PANDA model.

Mesh identifier	Azimuthal θ (number cells)	Vertical z [mm] (above/below sparger)	Radial r [mm] (max-min)	Number of cells
N_θ 64 Δz 50	64	50/**50**	25-100	210.000
N_θ 64 Δz 25	64	50/**25**	25-100	260.000
N_θ 64 Δz 12	64	50/**12**	25-100	440.000
N_θ 128 Δz 25	**128**	50/25	25-100	540.000
N_θ 128 Δz 12	**128**	50/**12**	25-100	990.000

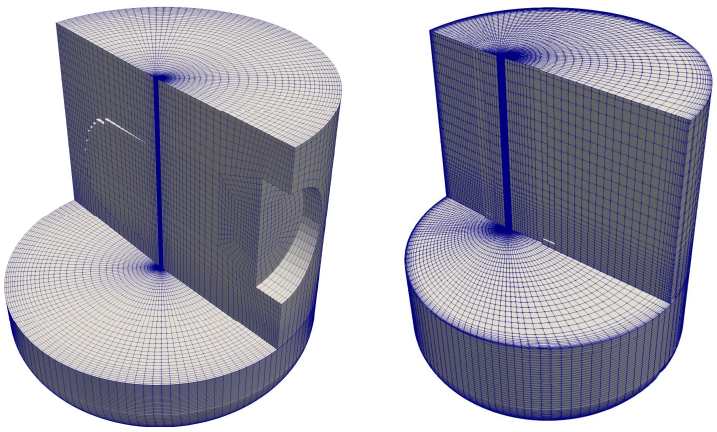

(a) (b)

Figure 11: Over-view of the N_θ 128 Δz 25 mesh (Table 2) used in the (a) PANDA and (b) PPOOLEX models. Note the off-centered location of the sparger in PPOOOLEX.

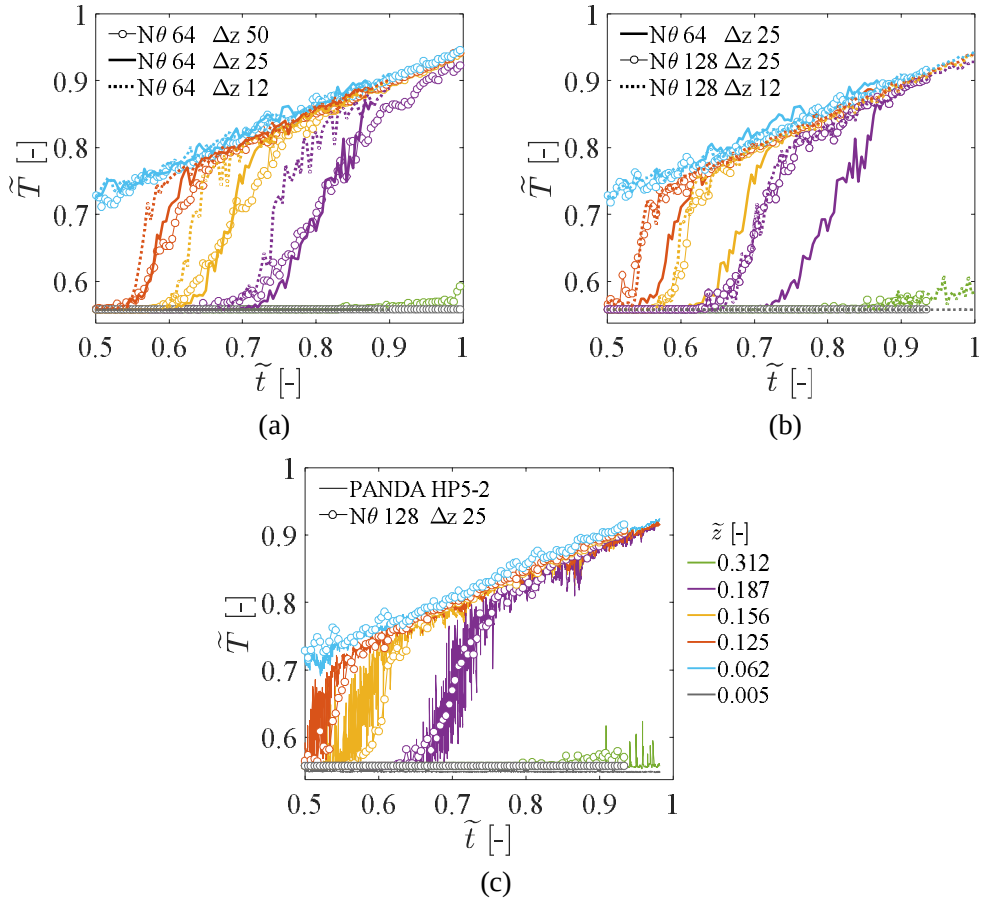

Figure 12: Mesh sensitivity study of the cell sized in the (a) vertical and (b) azimuthal directions and (c) comparison between PANDA HP5-2 data and the N_θ 128 Δz 25 mesh.

4.1. Sensitivity to injection conditions

Analysis of the TC and PIV data done in [1] shows that the sparger jets had a downwards inclination caused by the downwards steam velocity inside the sparger. The injection angle α (not to be confused with the *entrainment* angle discussed in Section 3.5) is an important variable since it determines the fraction of momentum driven towards the cold layer. Though the angle was estimated to be about 10° in [1], small variations were observed to cause significant changes on the pool behaviour (Figure 13). The largest effect was observed during the high steam injection phases, where an angle of 20° was able to erode the cold layer much faster than 0°. The angle effect was lower in the low steam injection phase, where we can see that larger angles caused a minor increase of the cold layer erosion rate (Figure 13a).

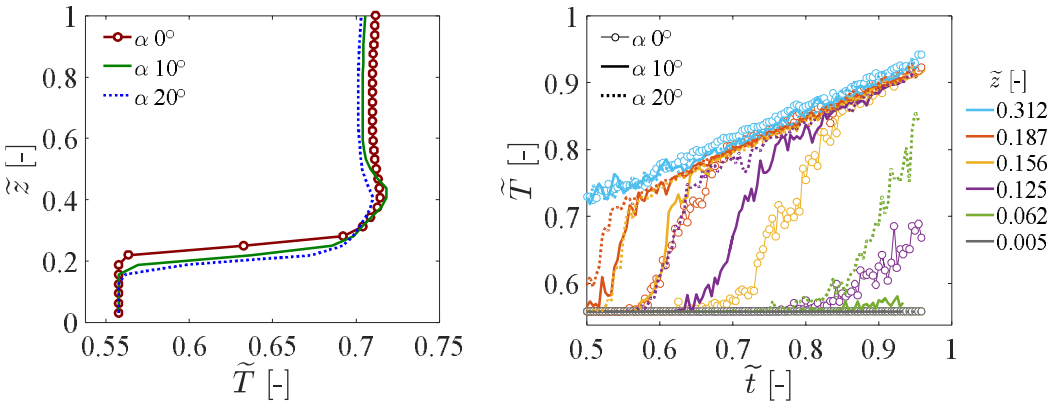

(a) (b)

Figure 13: Effect of the injection angle α on the pool behavior. (a) Temperature profile during the low steam injection phase, $\tilde{t}$ = 0.42 and (b) temperature evolution during the high steam injection phase.

Variations of the EMS velocity profile were also observed to cause changes of the pool response. In [1], the liquid jet induced by the steam injection was modelled with a Gaussian shape according to the PIV data based on

$$U = \frac{0.1}{x}\exp\left(-K\frac{r^2}{x^2}\right) \tag{18}$$

where x and r are the axial and radial coordinates, respectively, and K controls the standard deviation of the distribution and therefore the slenderness of the profiles. Although best agreement with the PIV data was obtained by using K = 40, a sensitivity study using K = 20 and 10 (Figure 14) showed that the erosion velocity is significantly decreased as K is reduced (Figure 15). It should be noted that the total momentum injected into the pool is the same for all the simulations while only the slenderness of the velocity profile changes. The low steam injection phase was also observed to be sensitive to changes in K although to a lesser extent than the high steam injection phase.

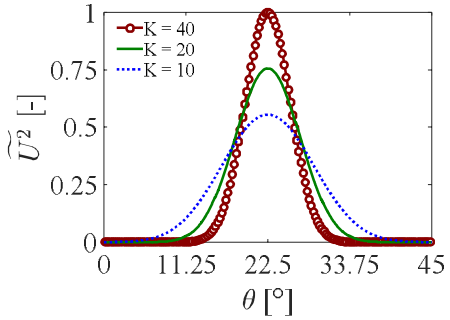

Figure 14: Momentum profiles at x = 0.1 m obtained with different K values in equation (18). Heat was distributed using the same profile. Detail of a single column initially containing 4 single jets which have merged into one resulting jet.

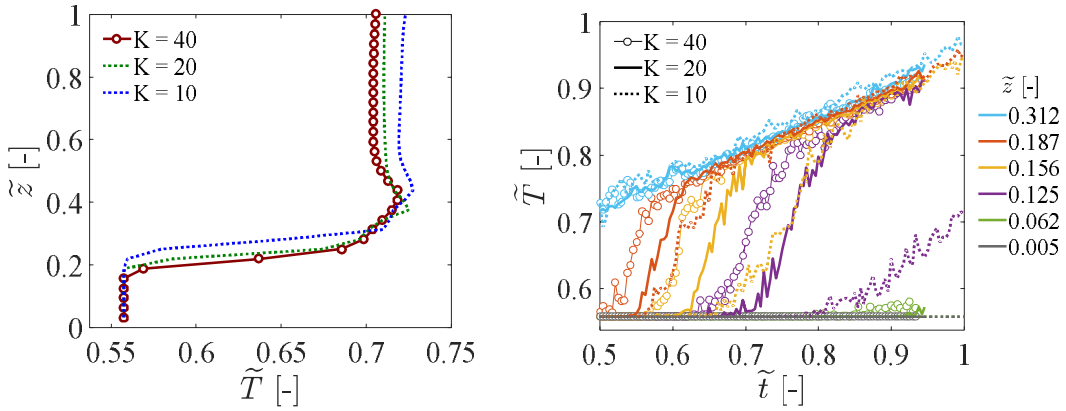

(a) (b)

Figure 15: Effect of the slenderness of the momentum and heat profile onto the temperature and the erosion of the pool. (a) Temperature profile during the low steam injection phase, $\tilde{t}$ = 0.42 and (b) temperature evolution during the high steam injection phase.

Analysis of the PIV data done in [1] shows that the turbulence intensity near the injection holes reached maximums of about 90 %. The turbulence viscosity could not be estimated due to the large errors propagated to this quantity.

The effect of the turbulence in the simulations was addressed by defining source terms of k and ω around the sparger, at the locations where the EHS and EMS are imposed. These sources are added to the turbulence field already generated by the velocity and temperature gradients, which reached turbulent viscosity ratios (ν_T/ν_L) of about 3000 near the sparger (Figure 4b). We can see in Figure 16 that the case with ν_T/ν_L of 12000 led to a slower erosion of the cold layer during the low and high steam injection phases. This was caused by the larger diffusion of the jets around the sparger; an analogous behaviour to lowering the K parameter for the momentum profile. A lower ν_T/ν_L source of 6000 led to very similar results to those with no source (ν_T/ν_L = 0) in both the low and high steam injection phases. This suggests that the turbulence generated by the flow was similar in magnitude to the one added in the source. The faster erosion compared to ν_T/ν_L = 0, mainly at $\tilde{z}$ = 0.125, suggests that small enough turbulent sources could avoid the diffusion of the jets near the sparger while propagating a larger ν_T/ν_L towards the thermocline (causing a faster erosion).

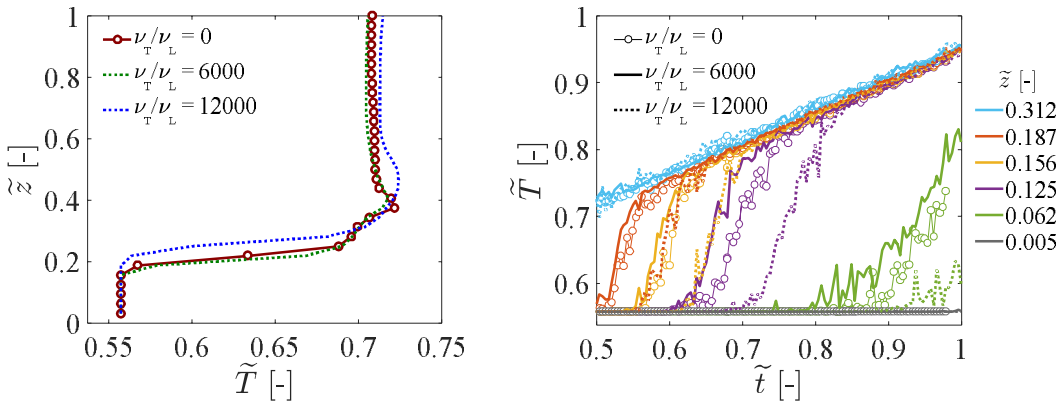

(a) (b)

Figure 16: Effect of the turbulent source at the sparger injection. Turbulence intensity of 80% in all the simulations, only the turbulent viscosity ratio ν_T/ν_L is varied. (a) Temperature profile during the low steam injection phase, $\tilde{t}$ = 0.42 and (b) temperature evolution during the high steam injection phase.

From this section, we can conclude that predicting the pool behaviour requires the following information for the momentum source: the absolute value given by equation (6), the injection angle, profile and turbulence sources. Based on the experimental data, the angle and profile could be estimated to be about α = 10° and K = 40 respectively. However, we have seen that variations from these values can cause significant changes in the transient pool behaviour. Therefore, the estimates of effective momentum presented in Section 4.2 should be considered as the best possible estimates considering the uncertainty in the experimental data.

4.2. Calibration of the momentum sources

The condensation regime coefficients C estimated with the simulations are presented in Figure 17 and Figure 18. All simulations predicted that C increases with the pool temperature T_p (or, equivalently, C increases as the subcooling $\Delta T = T_{sat}$-T_p is reduced).

During the low momentum steam injection phases (which is labelled as *stratification phases* in Figure 17), best agreement with the experiments was found when using C values between 0.20 and 0.45 for both the PANDA and PPOOLEX experiments. In contrast to this, the similarity between PANDA and PPOOLEX with respect to the C values does not hold true for the high steam injection phases. For example, despite the PANDA HP5-1 and PPOOLEX SPA-T3 were run with the same steam mass flux G and the same pool temperature T_p, the estimated C values are different: $C \approx 0.5$ for PANDA and $C \approx 1$ for PPOOLEX. The present C values obtained for the PPOOLEX experiments through calculations with ANSYS FLUENT are partially supported by previous simulations conducted with GOTHIC [31], where, despite using different modelling approaches (mesh, turbulence models, numerical schemes, etc.), similar C values were obtained. The difference between PPOOLEX and PANDA could be attributed to the uncertainty introduced by the modelling options and boundary conditions discussed in Sections 3 and 4.1. However, since the modelling approaches were the same for all the simulations, the difference could also be attributed to a physical phenomenon.

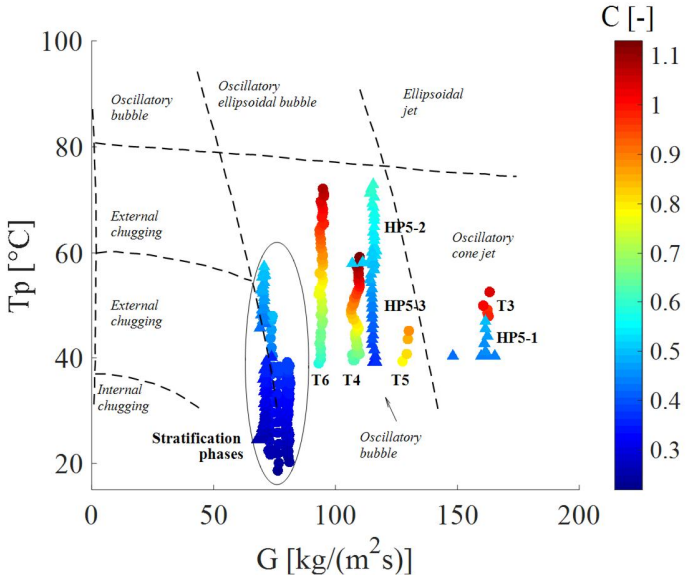

Figure 17: Condensation regime coefficient C estimated in the simulations as a function of the condensation regime map from Chan & Lee [28]. Symbols correspond to ▲ PANDA and ● PPOOLEX.

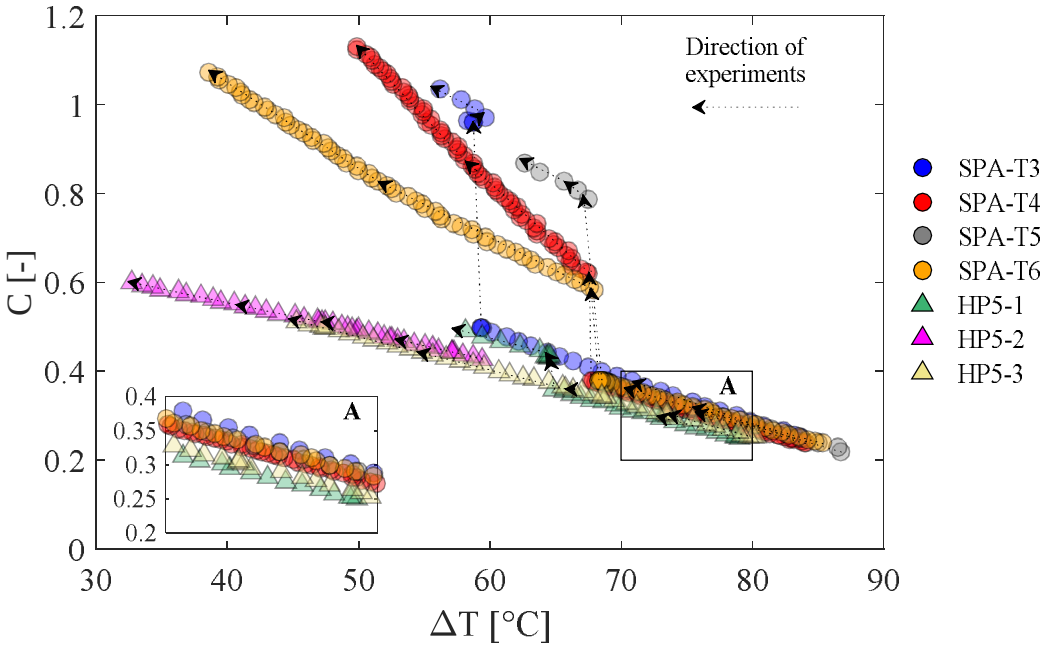

Figure 18: Condensation regime coefficient C estimated in the simulations as a function of the sub-cooling $\Delta T = T_{sat}$-T_p. Symbols correspond to ▲ PANDA and ● PPOOLEX.

The PPOOLEX and PANDA chugging experiments discussed in [1] were run at similar conditions, in terms of steam mass flux G and pool temperature T_p. However, in the PPOOLEX experiments the characteristic low frequency and high amplitude chugging oscillations were found; whereas the PANDA results indicated an intermittent bubble collapses of higher frequency and lower amplitude. These results suggest that different injection conditions of steam mass flux G and the pool temperature T_p may have also resulted in

different condensation regimes between the facilities (causing the need of different C coefficients). Another experimental observation is the difference between PPOOLEX and PANDA with respect to the Richardson scaling as discussed in [1]. In PANDA, the erosion velocity of the cold layer was significantly decreased as the distance between the sparger and cold layer increased. In some of the PPOOLEX experiments, the velocity was observed to be constant despite the increase of this distance.

Assuming that the differences in C presented in Figure 17 and Figure 18 are due to physical phenomena, the possible options which may have caused these differences can be summarized as follows.

- Geometry: Different geometrical parameters of the sparger were the diameters of the injection holes (8 mm in PPOOLEX, 9.5 mm in PANDA) and the inner diameter of the sparger pipe (68 mm in PPOOLEX, 81 mm in PANDA) [1]. According to [25], such differences should not lead to noticeable changes in the condensation regime. However, they could have caused changes in the injection angle and momentum profile, leading to significant differences in terms of erosion velocities as demonstrated in Figure 13 and Figure 15. In PANDA the sparger was located in the centre of the pool, whereas in PPOOLEX it was closer to the walls. This difference could have also led to a different entrainment pattern towards the jet region, modifying the total momentum magnitude or angle.

- Air volume fraction in the pool: The PANDA pool was de-gassed prior to the experiments to enabled the use of PIV in front of the injection holes. The resulting air volume fraction was about 3 times less than in atmospheric conditions. The reduction of air bubbles with respect to PPOOLEX can be observed in (Figure 19). The air volume fraction plays a very important role when injected together with steam (see PANDA HP5-5 experiment [1]). However, the importance of the volume fraction in the liquid phase has not yet been addressed in the literature.

- Vessel pressure: All the PPOOLEX experiments were pressurized (no relief valve during the transient), whereas the PANDA experiments were run at atmospheric conditions. This resulted in similar initial conditions, which could be the reason for the similarity of C during the low steam injection phases, which later led to larger steam pressures and temperatures in PPOOLEX (about 10 kPa larger). Work done by [43] shows that, for the same injection rates, a pressurized vessel leads to a stronger thermal stratification in the pool. This effect was attributed to the changes on the steam density, an effect which is already taken into account in the EMS sparger model, equation (6).

- Turbulence. Analysis of the experiments performed in [1] suggests that the erosion of the cold layer is governed by intermittent break-up of turbulent eddies and waves at the thermocline. Modelling the erosion with an equivalent turbulent viscosity seems to give a good qualitative agreement with the experiment (see Section 4.3). However, it is possible that differences between the facilities (proximity to the wall, vessel diameter, etc.) led to different turbulence propagation down to the stratified layer which could not be captured using a RANS approach.

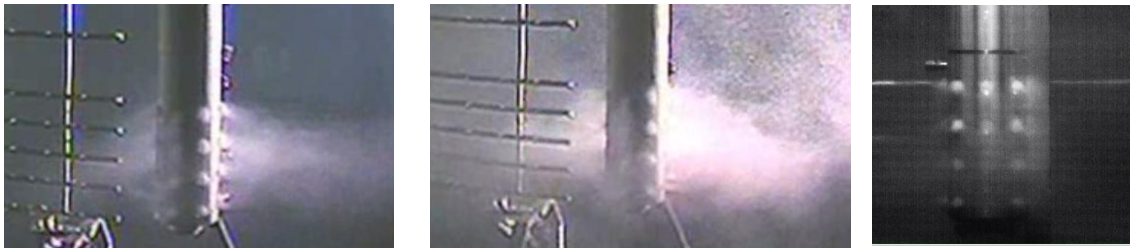

(a) (b) (c)

Figure 19: Snapshot of the video images obtained in the (a) low and (b) high steam injection phases of the PPOOLEX SPA-T4 and (c) low steam injection phase of PANDA HP5-2.

The temperature evolutions obtained in the simulations using the C coefficients from Figure 17 are presented in Figure 20, Figure 21, Figure 22 (PANDA) and Figure 23, Figure 24, Figure 25, Figure 26 (PPOOLEX). In general, it can be concluded that the modelling approach presented in Sections 2 and 3 can successfully reproduce the pool behaviour for a broad range of injection conditions and for different scales. All the low steam injection phases were well captured in terms of the location of the cold layer and the sharp gradient across the thermocline. In addition, the gradient across the thermocline was maintained during the erosion transients of the high steam injection phases. The deviations of the calculations from the experimental data became larger in the slow erosion transients of the PPOOLEX SPA-T4 and T6 (Figure 24, Figure 26). An improvement of those calculations could be done through further calibration of the C coefficients.

None of the simulations showed the *low frequency* oscillations of the thermocline layer observed in the experiments [1]. Despite this, the erosion velocities and trends were adequately predicted by the code. This indicates that the low frequency oscillations do not have an effect on the erosion of the cold layer, and that it is not crucial to capture them if the goal is to model the global pool temperature fields. The reason why the oscillations were not captured could be attributed to mesh resolution [1]. However, the simulations presented in Figure 12 show that the 12 mm mesh did not result in an improvement compared to 25 or 50 mm cells. Large Eddy Simulation (LES) could be used to determine if it is due to the RANS averaging.

As it was discussed in [1], the slow erosion of the cold layer is expected to be dominated by *high frequency* turbulent eddies splashing and creating unstable waves at the thermocline. The RANS approach is clearly not capable of resolving the turbulent eddies. However, the turbulent viscosity generated by the k-ω BSL model in combination with the proposed correlation for the $C_{3\varepsilon}$ parameter (equations (16) and (17)) seems to be well capable of modelling the behavior of the eddies. Therefore, it is considered that LES model would not be required to simulate the effect of these high frequency oscillations on stratification and mixing.

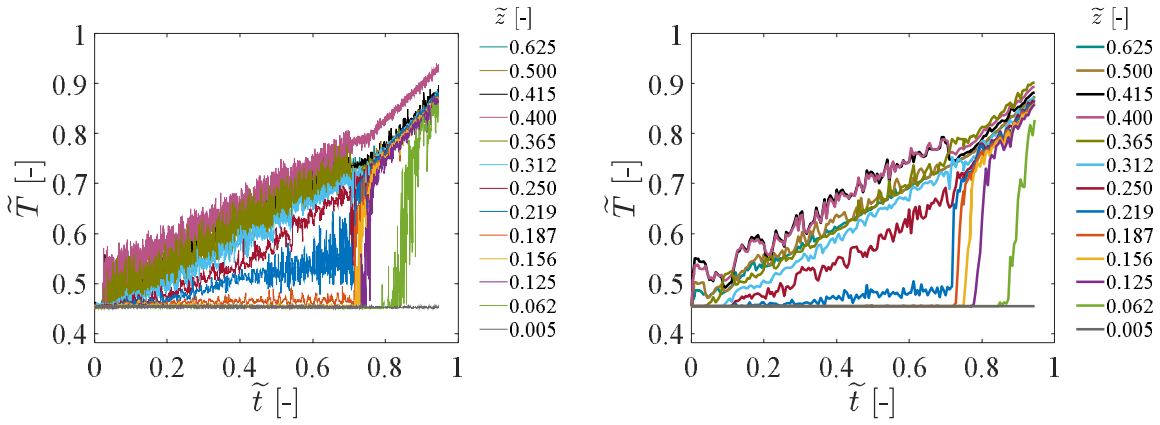

(a) (b)

Figure 20: PANDA HP5-1 (a) experiment and (b) Fluent simulation using the EHS/EMS models with the C coefficients from Figure 17. Temperature evolution along a vertical line of TCs in the pool.

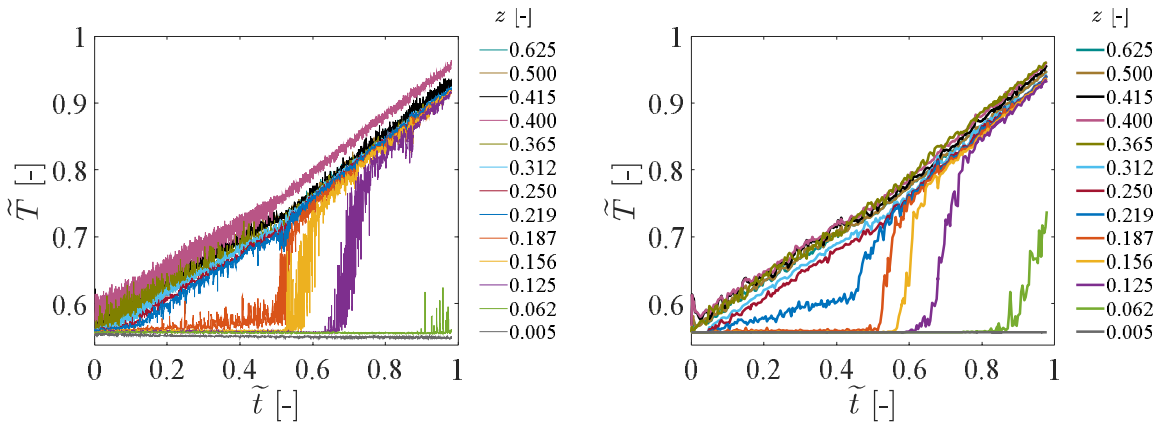

(a) (b)

Figure 21: PANDA HP5-2 (a) experiment and (b) Fluent simulation using the EHS/EMS models with the C coefficients from Figure 17. Temperature evolution along a vertical line of TCs in the pool.

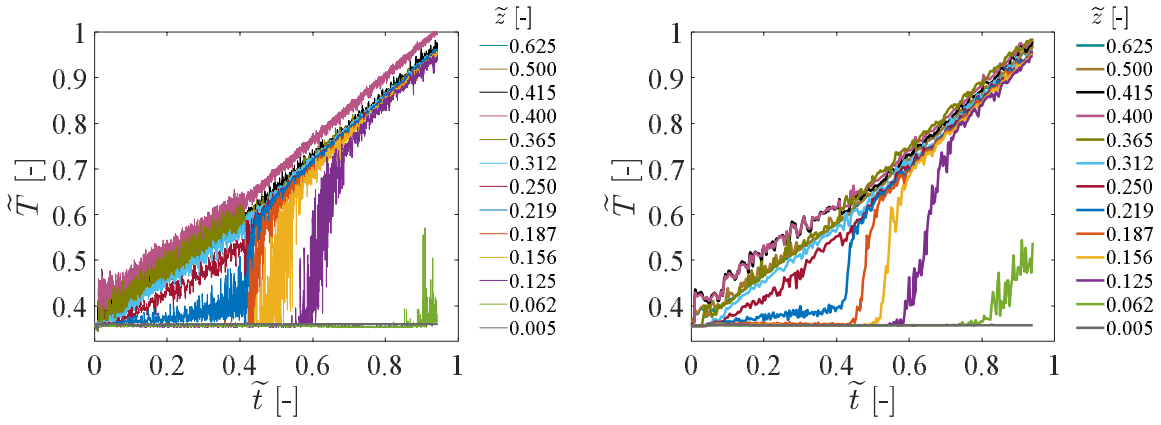

(a) (b)

Figure 22: PANDA HP5-3 (a) experiment and (b) Fluent simulation using the EHS/EMS models with the C coefficients from Figure 17. Temperature evolution along a vertical line of TCs in the pool.

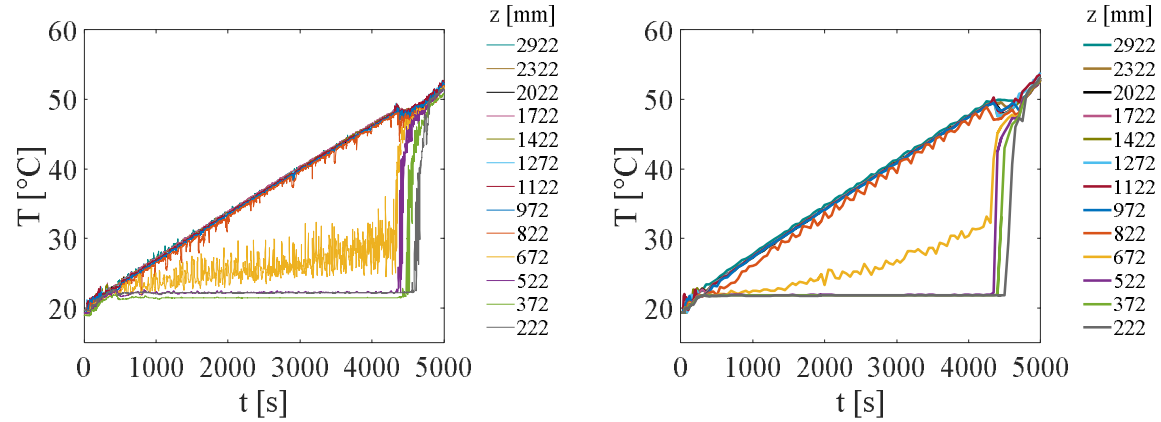

(a) (b)

Figure 23: PPOOLEX SPA-T3 (a) experiment and (b) Fluent simulation using the EHS/EMS models with the C coefficients from Figure 17. Temperature evolution along a vertical line of TCs in the pool.

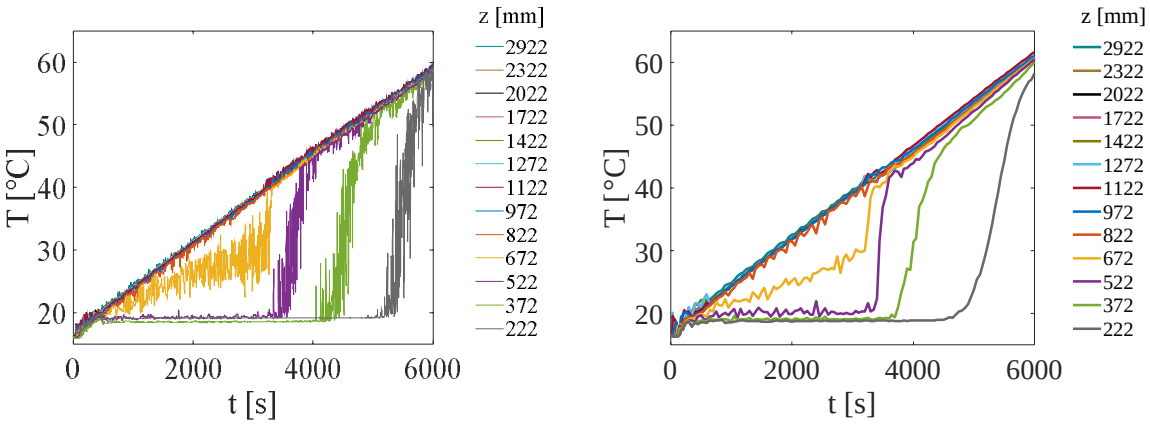

(a) (b)

Figure 24: PPOOLEX SPA-T4 (a) experiment and (b) Fluent simulation using the EHS/EMS models with the C coefficients from Figure 17. Temperature evolution along a vertical line of TCs in the pool.

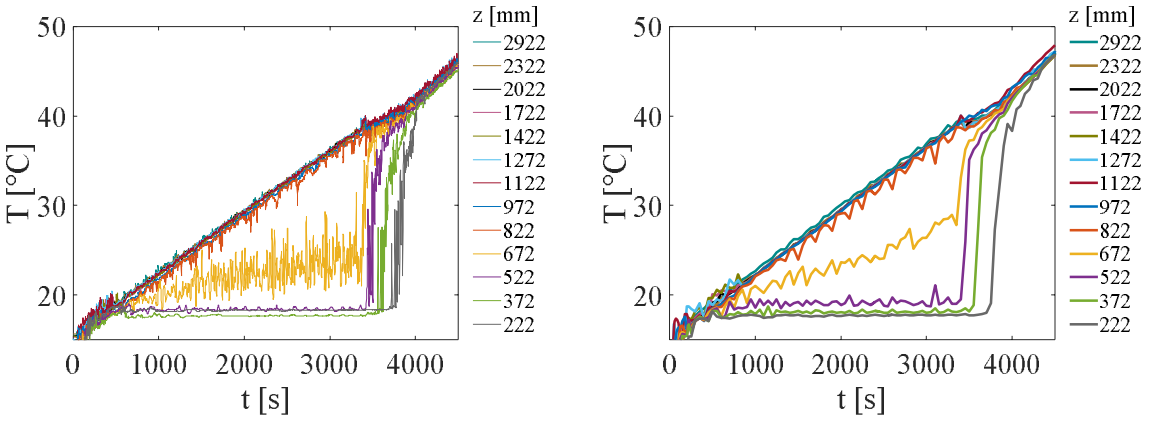

(a) (b)

Figure 25: PPOOLEX SPA-T5 (a) experiment and (b) Fluent simulation using the EHS/EMS models with the C coefficients from Figure 17. Temperature evolution along a vertical line of TCs in the pool.

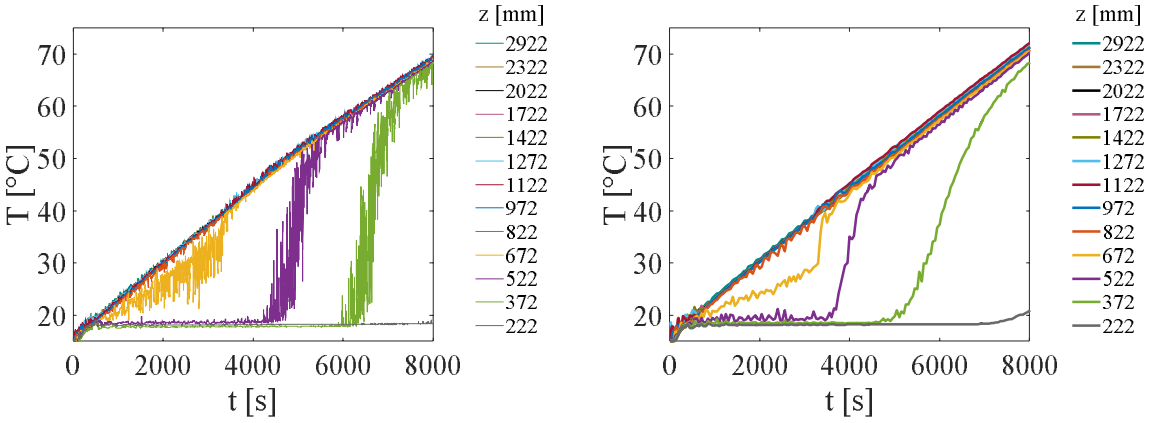

Figure 26: PPOOLEX SPA-T6 (a) experiment and (b) Fluent simulation using the EHS/EMS models with the C coefficients from Figure 17. Temperature evolution along a vertical line of TCs in the pool.

The velocity profiles obtained in the PANDA experiments and simulations are compared in Figure 27 and Figure 28 for low and high momentum steam injection phases. Due to the highly unsteady flow patterns and condensation regimes, the experimental data show a significant variation of the velocity profiles for similar condensation regimes [42], making it difficult for a direct comparison with the simulation. Nevertheless, we can see that the buoyancy driven and inertia dominated jets predicted for the low and high steam injection phases are in good agreement with the experiment. Similar to what was discussed in [1], the PIV data shows that the 4 individual jets located along the $\tilde{z}$ direction merged quickly past a non-dimensional distance of ≈0.2 into a single jet; proving that modelling a column jets using a single momentum source is adequate. The velocity magnitude also shows a good agreement with the experiment, indicating that the velocity profile used in the azimuthal direction (equation (18)) provides an adequate estimate.

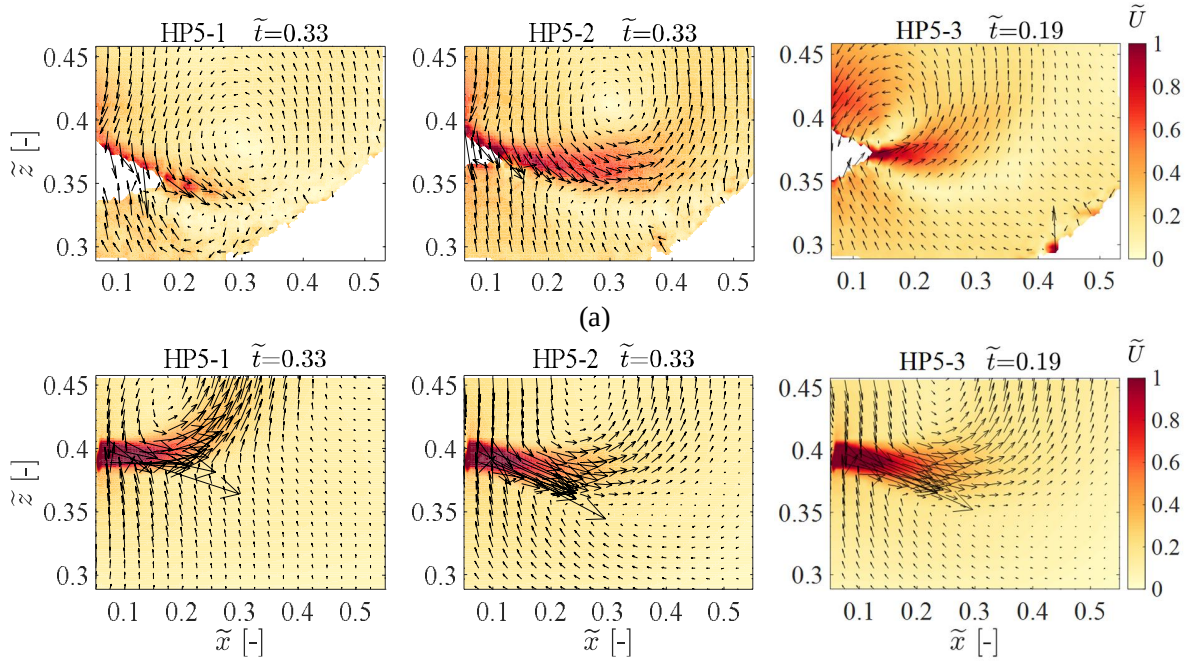

Figure 27: Velocity contours during the low steam injection phases obtained in the (a) PANDA HP5 experiments (PIV) and (b) Fluent simulations. All data plots have been time-averaged over 200 s.

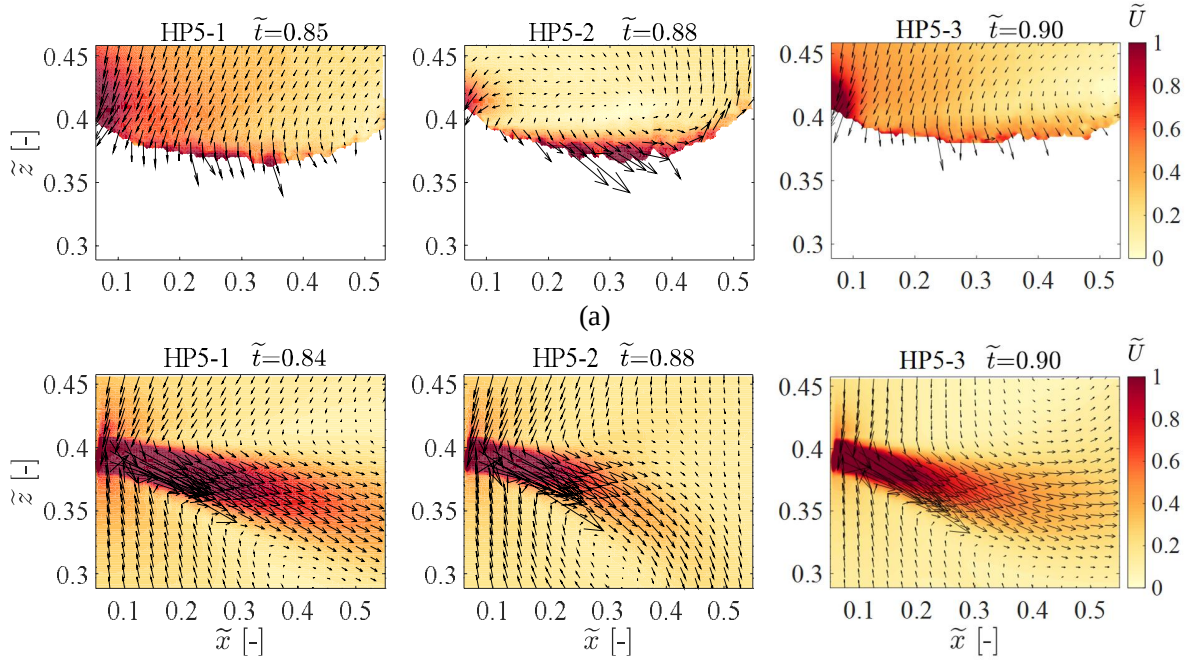

Figure 28: Velocity contours during the high steam injection phases obtained in the (a) PANDA HP5 experiments (PIV) and (b) Fluent simulations. All data plots have been time-averaged over 200 s.

4.3. Analysis of the flow above the thermocline

In this section we present a brief analysis of the calculated flow above the thermocline. This is done to determine what was the *main* driver of erosion of the cold layer in the simulations: shear flow or turbulence effects.

The turbulent viscosity ratio ν_T/ν_L and flow velocity U above the thermocline were estimated with a spatial average of all cell values located 300 mm above the layer with largest mean temperature gradient in the vertical direction (Figure 29). Assessment of which parameter has the dominant effect in the erosion velocity was done using the Reynolds number (momentum to viscous stresses), but using the turbulent viscosity instead of the laminar (kinematic) one. The length scale used in the Reynolds number was the pool diameter. As we can see in Figure 17, the Reynolds number reaches values of 100-300 during the erosion phases, suggesting that turbulence could be the largest contributor to the erosion. This assumption is based on the fact that the transition Reynolds number for laminar/turbulent flow is between 1000-3000.

Comparison between the pool temperature evolution presented in Section 4.2 and the ν_T/ν_L ratios from Figure 29 shows that the erosion velocity of the cold layer is well correlated with the ν_T/ν_L ratios. For example, the fast erosion of the HP5-1 and SPA-T3 simulations (Figure 20, Figure 23) resulted in similar initial ν_T/ν_L ratios of about 600. The decrease of ν_T/ν_L at the last stages of the HP5-1 correspond to the decrease in the erosion velocity, which was not able to mix the pool as in the SPA-T3. On the other hand, the slower erosion of the SPA-T6 experiment (Figure 26) shows ν_T/ν_L ratios of about 150. This correlation between turbulence and erosion velocity suggests that turbulence was the main driver of the erosion.

Another important aspect from Figure 17 is that, despite different C coefficients were needed for PPOOLEX and PANDA, the turbulent viscosity was similar in both cases for a given erosion velocity. This implies that although different momentum magnitude, angle or profile could be needed for each facility, the erosion velocity in both facilities is ultimately governed by the combined effect of these parameters on the amount of turbulence propagated down to the thermocline.

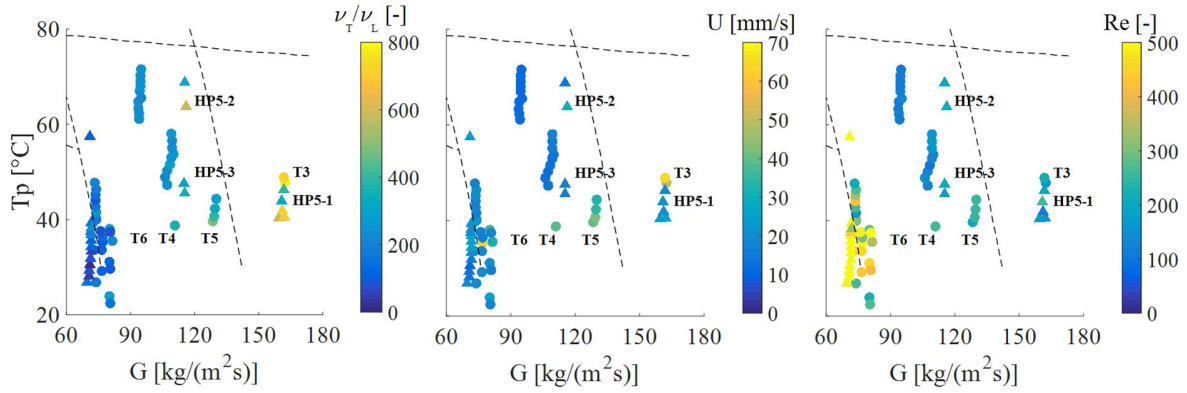

(a) (b) (c)

Figure 29: Mean value of the (a) turbulent viscosity ratio and (b) flow velocity and (c) Reynolds number 300 mm above the thermocline as a function of the condensation regime map from Chan & Lee [28]. Further details of the regime map can be observed in Figure 17. Symbols correspond to ▲ PANDA and ● PPOOLEX.

5. CONCLUSIONS

The prediction of the pool behavior during a steam injection is needed to address the containment performance during an accident. The large-scale and long-term nature of these transients make computational efficiency a necessity for the computational tools used for the prediction of these scenarios. This efficiency can be achieved with the Effective Heat Source (EHS) and Effective Momentum Source (EMS) models, where the small temporal and spatial scales of direct contact condensation are not resolved, but only their effect on the large-scale pool circulation. In this work, we have shown that the EHS/EMS models and their implementation in ANSYS Fluent 17.0 can be used to predict the pool behavior observed in the PPOOLEX and PANDA experiments with spargers. Modelling guidelines needed to simulate these types of transients have been established and are summarized below:

- Eulerian-Eulerian models such as VOF are not adequate for transients where buoyancy forces in the largest density phase (liquid pool in our case) are of interest. This is due to the reference density, which has to be specified equal for both phases. Thus, single-phase modelling of the pool is recommended. Transients with significant liquid level increase can use the dynamic layering option available in Fluent.
- The Boussinesq approximation for buoyancy should be implemented with a variable thermal expansion coefficient. A temperature-dependent density avoids restricting the simulations to the Boussinesq assumption, allowing for wider applicability to different transients.
- The turbulent dissipation at the thermocline is best modelled when using the k-ω BSL and a newly proposed dependency of the $C_{3\varepsilon}$ parameter based on the local gradient Richardson number. Application of k-ε models and other correlations for $C_{3\varepsilon}$ showed an artificial diffusion of the thermocline caused by over-production of turbulent viscosity.

- The inter connecting pipe at the PANDA vessel was observed to cause significant asymmetries in the flow which requires a full 3D modelling.
- The momentum induced by the steam injection was included in the simulation by adding source terms in the transport equations. The Steam Condensation Region Model (SCRM) using a fixed 90^o entrainment angle was observed to erode the cold layer further than when using source terms.

Using these modelling guidelines, the simulation results showed that the erosion of the cold layer depends on the total magnitude of the effective momentum, its profile, angle and induced turbulent sources. The magnitude of the effective momentum was calibrated by fixing all other parameters to the estimated values derived from the experiments [1]. Best agreement was obtained when using an effective momentum proportional to steam momentum at the injection holes by a C coefficient varying between 0.2 and 1.2. The calibrated C coefficient varies inversely proportional to the subcooling.

Given the same steam injection conditions (in terms of steam mass flux and subcooling), similar C coefficients were obtained for PPOOLEX and PANDA for the low steam injection phases, but not for the high steam injection phases. This was attributed to possible differences in the condensation regime, induced by the specific geometry and experimental procedures used in each facility. Such differences may have resulted in different injection parameters of momentum profile, angle and turbulence source.

Similar turbulent viscosity ratios were observed in the PPOOLEX and PANDA simulations for a given erosion velocity. Thus, it is concluded that the slow erosion of the cold layer is mainly determined by the generation and propagation of turbulence towards the thermocline (rather than mean flow shear). The generation and propagation of the turbulence is affected by specific injection conditions (angle, profile, total magnitude and turbulent source).

Further experimental campaigns with direct measurement of the effective momentum and other injection parameters should be done to assess the adequacy of the calibrated C coefficients. Currently, the so called Separate Effect Facility (SEF) is being built at Lappeenranta University of Technology (LUT), Finland, to provide a direct measurement of the effective momentum induced by prototypic steam condensation regimes occurring in a sparger.

ACKNOWLEDGEMENTS

The authors are grateful to the Swedish Radiation Safety Authority (SSM) for funding the Swedish participation in the OECD/NEA HYMERES project. The authors would like to thank the secretariat and all the members of the Management Board and the Programe Review Group of the HYMERES project for their help in defining the test programe and evaluating the test results.

The simulations were performed on resources provided by the Swedish National Infrastructure for Computing (SNIC) at PDC Centre for High Performance Computing (PDC-HPC). The authors are grateful to the PDC-HPC staff for assistance concerning the implementation aspects in making the code run on the PDC-HPC resources.

REFERENCES

1. Gallego-Marcos, I., Kudinov, P., Villanueva, W., Kapulla, R., Paranjape, S., Paladino, D., Laine, J., Puustinen, M., Räsänen, A., Pyy, L., Kotro, E., 2108. Pool Stratification and Mixing during a Steam Injection through Spargers: Analysis of the PPOOLEX and PANDA experiments. Nuclear Engineering and Design, 337, 300-316.

2. Pershagen, B., 1994. Light Water Reactor Safety. Pergamon Press, section 8.1.
3. Mizokami, S., Yamada, D., Honda, T., Yamauchi, D., Yamanaka, Y., 2016. Unsolved issues related to thermal-hydraulics in the suppression chamber during Fukushima Daiichi accident progressions. Journal of Nuclear Science and Technology, 53, 630-638.
4. Mizokami, S., Yamanaka, Y., Watanabe, M., Honda, T., Fuji, T., Kojima, Y., PAIK, C.Y., Rahn, F., 2013. State of the art MAAP analysis and future improvements on TEPCO Fukushima-Daiichi NPP accident. NURETH-15: The 15th International Topical Meeting on Nuclear Reactor Thermal Hydraulics, Pisa, Italy, May 12-17, paper number 536.
5. M., Pellegrini et al., 2016. Benchmark study of the accident at the Fukushima Daiichi NPS: best-estimate case comparison. Nuclear Technology 196, 198-210.
6. Li, H., Kudinov, P., 2010. Effective Approaches to Simulation of Thermal Stratification and Mixing in a Pressure Suppression Pool. OECD/NEA & IAEA Workshop CFD4NRS-3, September 14-16, 2010, Bethesda, MD, USA.
7. Li, H., Villanueva, W., Kudinov, P., 2014. Approach and Development of Effective Models for Simulation of Thermal Stratification and Mixing Induced by Steam Injection into a Large Pool of Water. Science and Technology of Nuclear Installations, 2014, Article ID 108782, 11 pages.
8. Li, H., Villanueva, W., Puustinen, M., Laine, J., Kudinov, P., 2014. Validation of Effective Models for Simulation of Thermal Stratification and Mixing Induced by Steam Injection into a Large Pool of Water. Science and Technology of Nuclear Installations, 2014, Article ID 752597, 18 pages.
9. Villanueva, W., Li, H., Puustinen, M., Kudinov, P., 2015. Generalization of experimental data on amplitude and frequency of oscillations induced by steam injection into a subcooled pool. Nuclear Engineering and Design, 295, 155-161.
10. Li, H., Villanueva, W., Puustinen, M., Laine, J., Kudinov, P., 2018. Thermal stratification and mixing in a suppression pool induced by direct steam injection. Annals of Nuclear Energy, 111, 487-498.
11. Gallego-Marcos, I., Villanueva, W., Kudinov, P., 2018. Modelling of Pool Stratification and Mixing Induced by Steam Injection through Blowdown Pipes. Annals of Nuclear Energy, 112, 624-639.
12. Laine, J., Puustinen, M., Räsänen, A., 2015. PPOOLEX Experiments with a Sparger, Nordic Nuclear Safety Research, NKS-334.
13. Paladino, D., Dreier, J., 2012. PANDA: A Multipurpose Integral Test Facility for LWR Safety Investigation. Science and Technology of Nuclear Installations, Article ID 239319, 9 pages.
14. Pättikangas, T.J.H., Niemi, J., Laine, J., Puustinen, M., Purhonen, H., 2010. CFD modelling of condensation of vapor in the pressurized PPOOLEX facility. OECD/NEA & IAEA Workshop CFD4NRS-3, 14-16 September 2010, Washington DC, USA.
15. Tanskanen, V., Jordan, A., Puustinen, M., Kyrki-Rajamäki, R., 2014. CFD simulation and pattern recognition analysis of the chugging condensation regime. Annals of Nuclear Energy, 66, 133-143.
16. Patel, G., 2017. Computational fluid dynamics analysis of steam condensation in nuclear power plant applications. Doctoral dissertation at Lappeenranta University of Technology, Finland.
17. Norman, T.L., Revankar, S.T., 2010. Jet-plume condensation of steam–air mixtures in subcooled water. Part 2: Code model. Nuclear Engineering and Design, 240, 533-537.
18. Kang, H.S., Song, C.H., 2008. CFD analysis for thermal mixing in a subcooled water tank under a high steam mass flux discharge condition. Nuclear Engineering and Design, 238, 492-501.
19. Kang, H.S., Song, C.H., 2010. CFD analysis of a turbulent jet behavior induced by a steam jet discharge through a single hole in a subcooled water tank. Nuclear Engineering and Design, 240, 2160-2168.
20. Moon, Y.T., Lee, H.D., Park, G.C., 2009. CFD simulation of a steam jet-induced thermal mixing into a subcooled water pool. Nuclear Engineering and Design, 239, 2849-2863.

21. Aya, I., Nariai, H., 1984. Chugging Phenomenon Induced by Steam condensation into pool water (amplitude and frequency of fluid oscillation). Translated from: Transactions of the Japan Society of Mechanical-Engineers, 50, 2427-2435.
22. Gamble, R.E., Nguyen, T.T., Shiralkar, B.S., Peterson, P.F., Greif, R., Tabata, H., 2001. Pressure suppression pool mixing in passive advanced BWR plants. Nuclear Engineering and Design 204, 321-336.
23. Kundu, P.K., Cohen, I.M., Dowling, D.R., 2011. Fluid Mechanics, fifth edition. Academic Press. Section 15.4.
24. Wu, X.Z., Yan, J.J., Li, W.J., Pan, D.D, Chong, D.T., 2009. Experimental study on sonic steam jet condensation in quiescent subcooled water. Chemical Engineering Science, 64, 5002-5012.
25. Song, C.H., Cho, S., Kang, H.S., 2012. Steam Jet Condensation in a Pool: From Fundamental Understanding to Engineering Scale Analysis. Journal of Heat Transfer, 134(3), 15 pages.
26. Heinze, D., Schulenberg, T., Behnke, L., 2015. A Physically Based, One-Dimensional Two-Fluid Model for Direct Contact Condensation of Steam Jets Submerged in Subcooled Water. Journal of Nuclear Engineering and Radiation Science, 1(2), 8 pages.
27. Malavasi, S., Messaa, G., Fratino, U., Pagano, A., 2012. On the pressure losses through perforated plates. Flow Measurement and Instrumentation, 28, 57-66.
28. Chan, C.K., Lee, C.K.B., 1982. A regime map for direct contact condensation. International Journal of Multiphase Flow, 8, 11-20.
29. Simpson, M.E., Chan, C.K., 1982. Hydrodynamics of a Subsonic Vapor Jet in Subcooled Liquid. Journal of Heat Transfer, 104(2), 271-278.
30. Yuan, F., Chong, D., Zhao, Q., Chen, W., Yan, J., 2016. Pressure oscillation of submerged steam condensation in condensation oscillation regime. International Journal of Heat and Mass Transfer, 98, 193-203.
31. Gallego-Marcos, I., Villanueva, W., Kudinov, P., 2016. Thermal Stratification and Mixing in a Large Pool Induced by Operation of Spargers, Nozzles, and Blowdown Pipes. Nordic Nuclear Safety Research, NKS-369.
32. ANSYS® Fluent Theory Guide, Release 17.0.
33. Fernando, H.J.S., 1991. Turbulent mixing in stratified fluids. Annual Review of Fluid Mechanics, 23, 455-93.
34. GOTHIC Thermal Hydraulic Analysis Package, Version 8.1(QA). EPRI, Palo Alto, CA: 2014.
35. Maele, K.V., Merci, B., 2006. Application of two buoyancy-modified k–ε turbulence models to different types of buoyant plumes. Fire Safety Journal, 41, 122-138.
36. Miles, J.W., 1961. On the stability of heterogeneous shear flows. Journal Fluid Mechanics, 10, 496-508.
37. Abarbanel, H.D., Holm, D.D., Marsden, J.E., Ratiu, T., 1984. Richardson Number Criterion for the Nonlinear Stability of Three-Dimensional Stratified Flow. Physical Review Letters, 52, 2352-2355.
38. De Silva, I.P.D., Brandt, A., Montenegro, L.J., Fernando, H.J.S., 1999. Gradient Richardson number measurements in a stratified shear layer. Dynamics of Atmospheres and Oceans, 30, 47-63.
39. Van Gastel, P., Pelegrí, J.L., 2004. Estimates of gradient Richardson numbers from vertically smoothed data in the Gulf Stream region. Scientia Marina, 68 (4), 459-482.
40. Gallego-Marcos, I., Villanueva, W., Kapulla, R., Paranjape, S., Paladino, D., Kudinov, P., 2016. Modeling of thermal stratification and mixing induced by steam injection through spargers into a large water pool. OECD/NEA & IAEA Workshop CFD4NRS-6, Cambridge, MA, USA, September 13-15, 2016.
41. Gallego-Marcos, I., Villanueva, W., Kapulla, R., Paranjape, S., Paladino, D., Kudinov, P., 2016. Scaling and CFD Modelling of the Pool Experiments with Spargers Performed in the PANDA Facility.

NUTHOS-11: The 11th International Topical Meeting on Nuclear Reactor Thermal Hydraulics, Operation and Safety Gyeongju, Korea, October 9-13, 2016. N11P0670.
42. R. Kapulla, D. Uong, C. Zimmer, D. Paladino, PIV measurements in the vicinity of a steam sparger in the PANDA facility, Nuclear Engineering and Design, article in press
43. Solom, M., Kirkland, K.V., 2016. Experimental investigation of BWR Suppression Pool stratification during RCIC system operation. Nuclear Engineering and Design, 310, 564-569.